Acta Materialia 235 (2022) 118056

Contents lists available at ScienceDirect

Acta Materialia

journal homepage: www.elsevier.com/locate/actamat

Short-range order and origin of the low thermal conductivity in compositionally complex rare-earth niobates and tantalates

Andrew J. Wright[a], Qingyang Wang[b], Yi-Ting Yeh[a], Dawei Zhang[c], Michelle Everett[d], Joerg Neuefeind[d], Renkun Chen[b,c], Jian Luo[a,c,*]

[a] Department of NanoEngineering, University of California San Diego, La Jolla, CA 92093, United States
[b] Department of Mechanical and Aerospace Engineering, University of California San Diego, La Jolla, CA 92093, United States
[c] Program of Materials Science and Engineering, University of California San Diego, La Jolla, CA 92093, United States
[d] Neutron Sciences Directorate, Oak Ridge National Laboratory, One Bethel Valley Road, Oak Ridge, TN 37831, United States

ARTICLE INFO

Article history:
Received 4 April 2021
Revised 15 May 2022
Accepted 21 May 2022
Available online 23 May 2022

Keywords:
Defect fluorite
High-entropy ceramics
Thermal conductivity
Rare-earth niobate
Young's modulus

ABSTRACT

Rare-earth niobates and tantalates possess low thermal conductivities, which can be further reduced in high-entropy compositions. Here, a large number of 40 compositions are synthesized to investigate the origin of low thermal conductivity. Of these, 29 possess single (nominally cubic) fluorite phases and most of them are new compositionally complex (medium- or high-entropy) compositions. Furthermore, doping 2% of light element cations can further reduce thermal conductivity. This large data set enables the discovery of a negative correlation between the thermal conductivity and averaged radius ratio of the 3+/5+ cations. While this ratio is still below the threshold for forming long-range ordered weberite-type phases, this correlation suggests the reduced thermal conductivity is related to short-range weberite-type order, which is indeed revealed by diffuse scattering in X-ray diffraction and neutron total scattering. Specifically, neutron total scattering is used to characterize five selected specimens. A better fit to a weberite-type structure is found at the nanoscale. The characteristic length (domain size) is appears to be larger in more insulative materials. As it approaches the Ioffe-Regel limit, the phonon limit breaks down and "diffusons" give rise to the observed amorphous-like thermal conductivity.

1. Introduction

Rare-earth (RE) niobates and tantalates (RE_3NbO_7 and RE_3TaO_7) are promising candidates for making the next generation thermal barrier coatings (TBCs) [1–6]. In general, developing new ceramic materials for TBCs is of critical importance for increasing the energy efficiency of gas-turbine engines [7,8]. Specifically, RE niobates and tantalates often form cubic "defect fluorite" structure (where RE^{3+} and Nb^{5+}/Ta^{5+} randomly occupy one cation sublattice, with a large fraction of 1/8th oxygen vacancies randomly distributed on the anion sublattice). An ordered weberite-type structure (of a $\sim\sqrt{2}\times\ \sim\sqrt{2}\times\ \sim 2$ supercell with respect to the original cubic fluorite unit cell) can also form with a large radius ratio of the 3+ RE cation to the 5+ Nb or Ta cation ($r^{3+}_{RE}/r^{5+}_{Nb/Ta}$) [2,9]. These RE_3NbO_7 and RE_3TaO_7 possess high melting temperatures (typically >2000 °C), low thermal conductivities ($k < 2\ W\ m^{-1}K^{-1}$), and moderate Young's moduli ($E \sim\ 200-250\ GPa$) [1–6].

In the last a few years, the field of high-entropy ceramics (HECs) is developing rapidly and attracting great scientific interest [10–12]. The majority of recent studies of HECs have been focused on rock salt [13–15], perovskite [16–19], and fluorite [20–25], pyrochlore [26–28] structured oxides, metal diborides [29–32], and rock salt carbides [33–37]. Recent work also explored other systems such as other borides (including monoborides [38], M_3B_4 borides [39], tetraborides [40], and hexaborides [41,42]), silicides [43–45], aluminides [46], nitrides [47,48], fluorides [49,50], silicates [51–54], and phosphates [55,56]. Notable properties of interest include enhanced electrochemical [12,57–60] and mechanical [29–31,35,37,61–64] performances. Significant modeling efforts have also made to help understand the experimental results or guide the exploration of new compositions [35,64–67]. More recently, we further proposed to broaden HECs to compositionally complex ceramics (CCCs), where non-equimolar and/or medium entropy compositions can outperform their equimolar high-entropy counterparts [10,22,26]. Defects (*e.g.*, aliovalent cation

* Corresponding author at: Department of NanoEngineering, University of California San Diego, La Jolla, CA 92093, United States.
E-mail address: jluo@alum.mit.edu (J. Luo).

https://doi.org/10.1016/j.actamat.2022.118056

doping or anion vacancies) and short- and long-range orders can bring additional complexity and opportunities to tailor the thermomechanical (and other) properties of these emerging HECs and CCCs [10,68].

Perhaps one of the most interesting and useful properties that HECs and CCCs possess, observed across nearly all systems examined, is represented by the reduced thermal conductivity [21–23,26,36,52,69–72]. Specifically, reduced and ultralow thermal conductivities have been shown in high-entropy RE niobates [10,23,68,73,74]. For example, in a 2020 perspective article [10], we reported the preliminary result for $(YDyErNb_{0.5}Ta_{0.5})O_7$ (k = 1.11 $W\,m^{-1}K^{-1}$; E = 226.5 GPa, NT1 in this study). Zhao et al. also reported the fabrication of high-entropy RE niobates and tantalates in 2020 (without reporting the thermal conductivity) [23]. A couple of recent articles in 2021 further reported ultralow thermal conductivities [73,74]. We also further investigated a series of single-phase duodenary oxides, *e.g.*, $[(Sm_{0.25}Eu_{0.25}Gd_{0.25}Yb_{0.25})_2(Ti_{0.5}Hf_{0.25}Zr_{0.25})_2O_7]_{1-x}[(Sc_{0.266}Dy_{0.248}Tm_{0.246}Yb_{0.240})_3NbO_7]_x$ with an order-disorder (pyrochlore-fluorite) transition, where one end-member is high-entropy RE niobates [68]. These recent studies collectively suggested that various high-entropy RE niobates and tantalates can be made into the (nominally cubic) fluorite structure (long-range order based on X-ray diffraction) with reduced and low thermal conductivities [10,23,68,73,74].

Braun et al. attributed low thermal conductivity in high entropy rock salt oxides to valency disorder inducing unit cell distortions [70]. Wright et al. showed the important roles of the concentration of oxygen vacancies and the size disorder in influencing the thermal conductivities in compositionally complex fluorite and pyrochlore oxides [22,26]. Here, we further investigate the underlying mechanisms of low thermal conductivities in high-entropy RE niobates and tantalates (including mixed niobates/tantalates).

In this study, we fabricated and investigated a large number of 40 RE niobates and tantalates (including 29 compositions that form single cubic phases), most of which are new compositionally complex (medium- and high-entropy) compositions not reported before. We examined the influence of the ratio of Nb and Ta and the effects of aliovalent doping. Notably, we discovered that the average $\overline{r_{RE}^{3+}}/\overline{r_{Nb/Ta}^{5+}}$ cation radii ratio controls the thermal conductivity. While the $\overline{r_{RE}^{3+}}/\overline{r_{Nb/Ta}^{5+}}$ ratios of our specimens are still well below the threshold for forming long-range ordered weberite-type phases, a negative correlation between the $\overline{r_{RE}^{3+}}/\overline{r_{Nb/Ta}^{5+}}$ ratio and thermal conductivity suggests the possible role of short-range weberite-type order, which was also evident by the diffuse scattering in X-ray diffraction. Furthermore, we employed advanced neutron total scattering, along with small-box modeling, to characterize selected specimens to confirm the existence of weberite-type short-range ordering at the nanoscale (~ 1 nm) suggested by King et al. [75]. Thus, the observed amorphous-like ultralow thermal conductivity is likely to due to a "diffuson" mechanism [76].

2. Experimental procedures

2.1. Materials synthesis and fabrication

Constituent binary rare-earth oxide, Al_2O_3, and MgO powders (particle sizes ~ 5 μm) were purchased from US Research Nanomaterials. CaO (particle size < 160 nm), Nb_2O_5 (particle size ~ 500 nm), and Ta_2O_5 powders were purchased from Sigma-Aldrich, SkySpring Nanomaterials, and Inframat Advanced Materials, respectively. The purity for all powders were > 99.9%. Note that the Al_2O_3, MgO, and CaO powders were used to dope a high-entropy tantalate that will be discussed in §3.3. Stoichiometric amounts of binary oxides were weighed out with a 0.01 mg precision for a total of 2 g. The powders along with 2 wt% stearic acid was added to a poly(methyl methacrylate) tube with tungsten carbide endcaps and one Ø5/16″ tungsten carbide ball. The powders were high-energy ball milled for 100 min (SPEX 8000D, SPEX SamplePrep, USA). The powders were then pressed under 100 MPa in a 0.5″ diameter stainless steel die and placed on a Pt foil for sintering at 1600°C or 1700°C for 24 h. Both surfaces of the specimens were ground with a 30 μm diamond disk to remove any surface contamination. Pellets were ground into a powder with an agate mortar and pestle for diffraction experiments.

2.2. Characterization

2.2.1. Phase, density, and compositional uniformity

X-ray diffraction (XRD, Miniflex II, Rigaku, Japan) was used to determine the crystal structure and theoretical density. Data was collected over 2 s per step with 0.02° 2θ steps at 30 keV. The bulk density was determined through the boiling method abiding the ASTM Standard C373–18 [77]. The relative density of the specimens ranged from 90 to 100%.

Scanning electron microscopy (SEM, FEI Apreo, OR, USA) with energy dispersive X-ray spectroscopy (EDS, Oxford N-Max^N) elemental mapping was used to characterize the compositional uniformity on cross-sectional specimens hot-mounted in acrylic (polished to 40 nm colloidal silica).

2.2.2. Neutron total scattering

Neutron total scattering experiments were carried out at Oak Ridge National Laboratory (ORNL) on the Nanoscale-Ordered MAterials Diffractometer (NOMAD, BL-1B) at the Spallation Neutron Source (SNS). Powders were loaded into a 2.8 *mm* ID, 3 *mm* OD diameter quartz capillary to a height of 3 *cm* (~ 0.7 *g*). The experiments were carried out at 290 *K* for a total accelerator proton charge of 8C, corresponding to about 92 min acquisition time at full power. The intensity from the detector bank 4 was used to show the neutron diffraction data. The data from all six detector banks were background-subtracted (from an empty quartz capillary) and normalized to the intensity of vanadium prior to being combined to produce the total scattering function, $S(Q)$. The data was also passed through a wavelength filter that excludes resonance as well as an absorption correction. This function was Fourier-transformed with a fixed $Q_{max} = 25$ Å^{-1} to obtain the neutron weighted pair distribution functions, $G(r) = r[g(r) - 1]$. The momentum transfer, Q, is given as $Q = 4\pi sin\theta/\lambda$, where θ and λ are the scattering angle and neutron wavelength. The Q_{damp} and Q_{broad} instrumental parameters were 0.017659 Å^{-1} and 0.0191822 Å^{-1}, respectively, that were determined from a Si standard.

2.2.3. Young's modulus (E)

The Young's modulus was determined through an oscilloscope (TDS 420A, Tektronix, USA) operating in pulse-echo mode following the ASTM Standard C1198–20 [78]. The longitudinal and transverse wave speeds and thus, Poisson's ratio and Young's modulus were calculated by the same method used in a previous publication [22].

The measured Young's modulus was corrected for porosity according to $E = \frac{E_{measured}}{1-2.9P}$, where P is the pore fraction [79]. All reported Young's moduli in this article are intrinsic materials properties extrapolated for fully dense specimens.

2.2.4. Thermal conductivity (k)

The thermal conductivity (k) was determined through the product of thermal diffusivity (α), density (ρ), and heat capacity (c_p). Laser flash analysis (LFA 467 *HT HyperFlash*, NETZSCH, Germany)

determined the thermal diffusivity. Before measurement, the specimens were coated with carbon to maximize laser absorption and infrared emission. The heat capacity was calculated through the weighted average of the heat capacity of the constituents [80] according to the Neumann-Kopp rule.

The measured thermal conductivity was corrected for porosity according $k = \frac{k_{measured}}{(1-P)^{3/2}}$, where P is the pore fraction [81]. Again, all reported thermal conductivities in this article are intrinsic materials properties that represent the values extrapolated for fully dense specimens (with the porosity effects being corrected/removed).

2.2.5. Scanning transmission electron microscopy (STEM)

A transmission electron microscopy (TEM) specimen of NT5–50 was prepared by a standard lift-out method using a focused ion beam (FIB). A double aberration-corrected scanning transmission electron microscope (STEM, JEOL JEM-ARM300CF, Japan) equipped with a high-angle annular dark-field (HAADF) detector operating at 300 kV was used to generate atomic resolution images and nanoscale energy dispersive X-ray spectroscopy (EDS) elemental maps.

2.3. Neutron total scattering modeling

A small-box modeling approach was carried out with the PDFgui software [82]. A cif file was created in VESTA for each composition based on a A_4O_7 defect fluorite (space group 225, $Fm\bar{3}m$) and A_3BO_7 weberite-type (space group 20, $C222_1$) unit cell [83]. The fluorite cell had the lattice parameter, scale, correlated atomic motion (delta2), and the isotropic atomic displacement parameter (ADP) for the cation and anion site refined (with five parameters in total). The weberite-type cell had 27 parameters refined, including: lattice parameters, scale, correlated atomic motion (delta2), eight ADPs corresponding to the eight distinct lattice sites, and 14 lattice position parameters. When applicable, the mixed A-/B-sites were refined all-in-same atomic site (*i.e.*, each cation on a mixed site were refined to have identical positions and U_{iso}). The fitting range was selected to be from 0.02 Å – 50 Å and the upper bound was then reduced in 5 Å steps until the final fitting range of 0.02 Å – 10 Å. After each fitting window, the converged parameters were used as initial values for the next round of fitting.

3. Results and discussion

3.1. Phase formation

Among 40 compositions examined in this study, 29 exhibit a single (nominally cubic) fluorite phase and one exhibit single (orthorhombic) weberite-type phase according to the benchtop XRD analysis. Among, 26 single-phase solid solutions can be classified as medium- or high-entropy compositions (with 4–6 different metal cations and $>1k_B$ per cation in the ideal mixing configurational entropy [10]). The key results of all 40 compositions are documented in Table S1, along with all XRD spectra (Supplementary Figs. S5–S13), in the Supplementary Material. The 29 single (nominally cubic) phase compositions and their room temperature thermal conductivity and Young's modulus are listed in Table 1. Selected SEM EDS elemental maps showing the compositional homogeneity are also documented in Supplementary Figs. S15 and S16.

Eight of the ten compositions that have secondary phases are those (non-conventional compositions) doped with 10% or more TiO_2, CaO, $AlO_{1.5}$ (= ½ Al_2O_3), and MgO (Supplementary Figs. S13a and S14). Another is the NT10 doped with 2% TiO_2 with a trace amount of a secondary phase (Fig. 2a). The only other two-phase composition is $Dy_3(Nb_{1/4}Ta_{3/4})O_7$, while Dy_3TaO_7 exhibits single orthorhombic weberite-type phase.

The other 29 conventional compositions with a variety of different RE combinations, including some doped with 2% CaO, $AlO_{1.5}$, and MgO, are single (nominally) cubic defect fluorite phase (for the long-range ordering based on XRD, albeit the possible existence of short-range weberite-type orders discussed later). Thus, this study suggests the ubiquitous formation of high-entropy RE niobates and tantalates.

3.2. Benchmark and influence of Nb:Ta ratio

In a 2019 study, Dy_3NbO_7 was reported to have a ultralow thermal conductivity of $k = 1\ W\ m^{-1}\ K^{-1}$ and the highest reported E/k ratio [84]. An interesting experiment is to investigate the influence of substituting Nb with Ta (as Ta is approximately twice the mass of Nb, while Ta and Nb have almost the same ionic radius of ~0.64 Å [85]). Interestingly, Dy_3NbO_7 has a fluorite structure while Dy_3TaO_7 has a (long-range ordered) weberite-type structure; thus, a disorder-order transition, which can occur gradually with a two-phase transition region, can influence the properties. A recent study [86] of $Dy_3(Nb_{1-x}Ta_x)O_7$ (x = 0, 1/6, 1/3, 1/2, 2/3, 5/6, and 1) found that the thermal conductivities are in the range of 1.1 $W\ m^{-1}\ K^{-1}$ for 100–900 °C, and both the modulus and thermal conductivity decrease with increasing Nb fraction. However, the fluorite-weberite transition complicates the interpretation.

Thus, we first investigated a similar series of compositions (NT0–0, NT0–25, NT5–50, NT0–75, and NT0–100 for x = 0, 0.25, 0.5, 0.75, and 1 in $Dy_3(Nb_{1-x}Ta_x)O_7$) as a benchmark. Our Dy_3NbO_7 (*i.e.*, NT0–0, also expressed as $(Dy_{0.75}Nb_{0.25})_4O_7$ to emphasize that Dy and Nb randomly occupy the same cation sublattice in a A_4O_7 defect-fluorite phase) has a measured thermal conductivity of $k = 1.10 \pm 0.03\ W\ m^{-1}\ K^{-1}$ (10% higher than that reported in Ref. [84] and comparable with that reported in Ref. [86]) and modulus of E = 201.8 ± 2.2 GPa. This yields a E/k ratio of 183.8 ± 2.8 $GPa\ m\ K\ W^{-1}$ (lower than that reported in Ref. [84]). The moderate differences may be attributed to the different measurements methods as well as the possible effects of residual porosity (while we note that our reported values represent intrinsic materials properties extrapolated for fully dense specimens). Overall, the agreements with literature are satisfactory, but we will focus on comparing the data obtained from our specimens fabricated and measured by the same procedure in most of the following discussion for consistence.

In our series of specimens, the thermal conductivity stays almost constant with increasing modulus for NT0–25 and NT0–50 with increasing Ta doping, producing higher E/k ratios of 188–189 $GPa\ m\ K\ W^{-1}$ (Fig. 1(b)). A (long-range) weberite-type phase started to form in $Dy_3(Nb_{1/4}Ta_{3/4})O_7$ (Fig. 1a), where both modulus E and conductivity k increase abruptly (Fig. 1(b)). The E/k ratio dropped substantially in the weberite-type Dy_3TaO_7 due to a higher k with slightly reduced E.

Next, we further investigated a series of compositionally complex $(Dy_{0.25}Er_{0.25}Ho_{0.25}Nb_{0.25-x}Ta_x)_4O_7$, which all show a single fluorite phase without long-range weberite-type ordering (Fig. 1(c)). The measured E, k, and E/k are shown in Fig. 1(d). Both the modulus and conductivity increase as more Nb is substituted for Ta (albeit an initial drop of modulus with a small amount of Ta substitution), similar to the simpler $Dy_3(Nb_{1-x}Ta_x)O_7$ series. Notably, both E and k increase substantially from x = 0.125 to x = 0.1875 (corresponding to a change in an increase in Ta fraction) without a phase (long-range disorder-order) transition (Fig. 1(d)). Interestingly, similar increases in E and k were observed in $Dy_3(Nb_{1-x}Ta_x)O_7$ accompanying a long-range ordering (fluorite-weberite phase transition) at the same Ta/(Nb+Ta) ratio (Fig. 1(b) and Ref. [86]). Thus, these analogous abrupt increases in E and k leads one to wonder if short-range weberite-type ordering is emerged in compositionally complex $(Dy_{0.25}Er_{0.25}Ho_{0.25}Nb_{0.25-x}Ta_x)_4O_7$, despite the absence of the

Table 1
The thermomechanical properties of each niobates and tantalates synthesized in this study sorted by $\overline{r^{3+}}/\overline{r^{5+}}$. Specimens examined by neutron diffraction are denoted by *.

Identifier	Composition	$\overline{r^{3+}}/\overline{r^{5+}}$	k_{RT} ($\frac{W}{m \cdot K}$)	E_{RT} (GPa)	E/k (GPa m K W^{-1})
NT8*	$(Sc_{0.25}Yb_{0.25}Lu_{0.25}Nb_{0.25})_4O_7$	1.281	1.28 ± 0.04	225.2 ± 2.3	176.3 ± 2.6
NT20	$(Sc_{0.168}Er_{0.234}Tm_{0.183}Yb_{0.165}Nb_{0.25})_4O_7$	1.316	1.24 ± 0.02	211.4 ± 1.9	170.7 ± 2.8
NT21	$(Sc_{0.2}Dy_{0.186}Tm_{0.185}Yb_{0.18}Nb_{0.25})_4O_7$	1.316	1.24 ± 0.02	214.1 ± 1.9	172.1 ± 2.6
NT24	$(Sc_{0.185}Dy_{0.21}Er_{0.182}Yb_{0.173}Nb_{0.25})_4O_7$	1.324	1.21 ± 0.05	217.9 ± 1.8	179.9 ± 2.9
NT25*	$(Sc_{0.165}Dy_{0.191}Ho_{0.197}Tm_{0.197}Nb_{0.25})_4O_7$	1.337	1.21 ± 0.03	217.8 ± 1.7	180.4 ± 3.2
NT10–2A	$(Er_{0.245}Tm_{0.245}Yb_{0.245}Al_{0.02}Ta_{0.245})_4O_{7-\delta}$	1.343	1.18 ± 0.04	209.0 ± 2.7	179.6 ± 3.4
NT10–2M	$(Er_{0.245}Tm_{0.245}Yb_{0.245}Mg_{0.02}Ta_{0.245})_4O_{7-\delta}$	1.347	1.20 ± 0.04	207.4 ± 2.7	177.6 ± 3.0
NT26	$(Sc_{0.15}Dy_{0.279}Ho_{0.171}Er_{0.15}Nb_{0.25})_4O_7$	1.347	1.16 ± 0.03	222.9 ± 1.9	191.4 ± 3.2
NT4*	$(Er_{0.25}Tm_{0.25}Yb_{0.25}Nb_{0.25})_4O_7$	1.356	1.15 ± 0.04	217.9 ± 2.5	190.1 ± 3.2
NT10	$(Er_{0.25}Tm_{0.25}Yb_{0.25}Ta_{0.25})_4O_7$	1.356	1.22 ± 0.04	226.5 ± 3.1	185.4 ± 3.4
NT6	$(Y_{0.25}Tm_{0.25}Yb_{0.25}Nb_{0.25})_4O_7$	1.363	1.19 ± 0.04	215.6 ± 2.5	180.8 ± 2.9
NT10–2C	$(Er_{0.245}Tm_{0.245}Yb_{0.245}Ca_{0.02}Ta_{0.245})_4O_{7-\delta}$	1.365	1.15 ± 0.03	204.1 ± 2.3	182.7 ± 2.8
NT2	$(Dy_{0.25}Er_{0.25}Yb_{0.25}Nb_{0.125}Ta_{0.125})_4O_7$	1.372	1.10 ± 0.03	223.9 ± 2.7	202.8 ± 3.3
NT5	$(Dy_{0.25}Ho_{0.25}Er_{0.25}Nb_{0.25})_4O_7$	1.388	1.09 ± 0.03	214.2 ± 2.4	196.0 ± 3.9
NT5–25	$(Dy_{0.25}Ho_{0.25}Er_{0.25}Nb_{0.188}Ta_{0.063})_4O_7$	1.388	1.11 ± 0.01	202.9 ± 2.2	182.4 ± 3.0
NT5–100	$(Dy_{0.25}Ho_{0.25}Er_{0.25}Ta_{0.25})_4O_7$	1.388	1.21 ± 0.01	222.4 ± 3.5	183.9 ± 3.4
NT5–75	$(Dy_{0.25}Ho_{0.25}Er_{0.25}Nb_{0.063}Ta_{0.188})_4O_7$	1.388	1.19 ± 0.01	224.2 ± 3.1	187.8 ± 3.2
NT5–50*	$(Dy_{0.25}Ho_{0.25}Er_{0.25}Nb_{0.125}Ta_{0.125})_4O_7$	1.388	1.12 ± 0.01	207.6 ± 2.7	184.8 ± 3.0
NT1	$(Y_{0.25}Dy_{0.25}Er_{0.25}Nb_{0.125}Ta_{0.125})_4O_7$	1.389	1.11 ± 0.03	226.5 ± 2.6	204.1 ± 3.1
NT5–50 2L	$(Dy_{0.245}Ho_{0.245}Er_{0.245}La_{0.02}Nb_{0.123}Ta_{0.123})_4O_{7-\delta}$	1.393	1.09 ± 0.01	222.7 ± 2.7	204.6 ± 3.3
NT3	$(Y_{0.25}Dy_{0.25}Ho_{0.25}Nb_{0.25})_4O_7$	1.395	1.14 ± 0.03	208.8 ± 2.2	182.7 ± 2.8
NT5–50 4L*	$(Dy_{0.24}Ho_{0.24}Er_{0.24}La_{0.04}Nb_{0.12}Ta_{0.12})_4O_{7-\delta}$	1.399	1.06 ± 0.01	220.6 ± 2.5	209.0 ± 3.4
NT32	$(Y_{0.143}Dy_{0.587}Ho_{0.02}Nb_{0.143}Ta_{0.107})_4O_7$	1.403	1.15 ± 0.06	226.7 ± 3.0	196.4 ± 3.4
NT5–50 6L	$(Dy_{0.235}Ho_{0.235}Er_{0.235}La_{0.06}Nb_{0.118}Ta_{0.118})_4O_{7-\delta}$	1.404	1.10 ± 0.01	218.9 ± 3.0	198.6 ± 3.7
NT0–0	$(Dy_{0.75}Nb_{0.25})_4O_7$	1.406	1.10 ± 0.03	201.8 ± 2.2	183.8 ± 2.8
NT0–25	$(Dy_{0.75}Nb_{0.188}Ta_{0.063})_4O_7$	1.406	1.11 ± 0.01	209.4 ± 2.4	188.4 ± 3.0
NT0–50	$(Dy_{0.75}Nb_{0.125}Ta_{0.125})_4O_7$	1.406	1.10 ± 0.01	207.6 ± 2.3	189.1 ± 2.9
NT5–50 8L	$(Dy_{0.23}Ho_{0.23}Er_{0.23}La_{0.08}Nb_{0.115}Ta_{0.115})_4O_{7-\delta}$	1.409	1.12 ± 0.01	201.3 ± 2.2	179.3 ± 2.7
NT5–50 10L	$(Dy_{0.225}Ho_{0.225}Er_{0.225}La_{0.1}Nb_{0.113}Ta_{0.113})_4O_{7-\delta}$	1.415	1.12 ± 0.01	208.8 ± 2.6	187.1 ± 3.0

long-range weberite-type order that occurs in the simpler composition of $Dy_3(Nb_{1-x}Ta_x)O_7$ with the Ta/(Nb+Ta) ratio greater than ¾.

3.3. Reducing thermal conductivity with light cation doping

As a new discovery, we further demonstrated that introducing a small amount of light element cations (Mg^{2+}, Al^{3+}, and Ca^{2+}) into a dense matrix of high-entropy tantalates, NT10 $(Er_{1/4}Tm_{1/4}Yb_{1/4}Ta_{1/4})_4O_7$, can further reduce the room temperature thermal conductivity while maintaining single high-entropy solid-solution phases.

The 2% MgO, $AlO_{1.5}$ (1/2 Al_2O_3), and CaO doped $(Er_{1/4}Tm_{1/4}Yb_{1/4}Ta_{1/4})_4O_7$ were the single fluorite phase according to XRD, while a trace amount of secondary phase was observed in 2% TiO_2 doped $(Er_{1/4}Tm_{1/4}Yb_{1/4}Ta_{1/4})_4O_7$ (Fig. 2(a)). In contrast, all the four 10% doped specimens had significant amounts of secondary phases (Supplementary Figs. S13a and S14). The modulus of all the specimens decreases with doping (see Fig. 2(c) for 2% doped compositions and all data in Supplementary Table S1), which may be due to aliovalent doping and oxygen vacancy effects. The thermal conductivity decreases at 2% doping of MgO, $AlO_{1.5}$, CaO, and TiO_2 (Fig. 2(c)). Most notably, 2% CaO doped $(Er_{1/4}Tm_{1/4}Yb_{1/4}Ta_{1/4})_4O_7$, which is single fluorite phase according to XRD (Fig. 2(a)), possesses appreciably reduced thermal conductivity at all temperature range in comparison with $(Er_{1/4}Tm_{1/4}Yb_{1/4}Ta_{1/4})_4O_7$ (Fig. 2(c)). In contrast, 2% doping of MgO, $AlO_{1.5}$, and TiO_2 reduces the room-temperature thermal conductivity, but increases the high-temperature thermal conductivity, of the $(Er_{1/4}Tm_{1/4}Yb_{1/4}Ta_{1/4})_4O_7$. The thermal conductivity increases significantly in the two-phase regime with 10% doping for all four light element oxide dopants (Supplementary Table S1).

The reduction of the room-temperature thermal conductivity with 2% of light cations Mg^{2+}, Al^{3+}, and Ca^{2+} in $(Er_{1/4}Tm_{1/4}Yb_{1/4}Ta_{1/4})_4O_7$ (without precipitating a secondary phases) represents an interesting new observation. This may suggest a "locon" effect (resulted from localized vibration modes of doped light element in a matrix of heavy elements) [76]. However, locons are usually the vibrational modes with the high frequency [76]. If it was the locon effect only, if would only impact the high frequency modes and would not impact the mechanical and acoustic properties (that are related to low-frequency modes). While the locon effect [76] remains a possible contributing mechanism, it is premature to draw a conclusion here. Instead, we hypothesize that the doping of the light element cations may have multiple effects. First, it does decease the Young's modulus, which will reduce phonon speed of sound (low frequency modes) and in turn decrease the thermal conductivity. Second, doping with light cations can increase the mass disorder (albeit that our correlation analysis shown in Supplementary Fig. S1(b) in suggests the opposite: *i.e.*, statistically, increased mass disorder surprisingly leads to slightly increased thermal conductivity in this class of materials). Third, some light element cations are also aliovalent, which can create charge defects and oxygen vacancies. In any case, the reduction of the thermal conductivity with small levels of light cations within the single high-entropy phases (Fig. 2(c)) represents an interesting finding (and perhaps a new direction to further tailor the thermomechanical properties of high-entropy niobates and tantalates).

The decreases in the thermal conductivities in 10% doped specimens are likely related to the formation of significant amounts of secondary phases (as shown in Supplementary Figs. S13a and S14) at the high doping level. These cases are too complicated and not sufficiently interesting to warrant further investigation. However, since the 10% doped specimens clearly exhibited secondary phases, we do not rule out the possibility that there may be some agglomeration in the 2% doped specimens that were undetectable by benchtop XRD and SEM-EDS analysis.

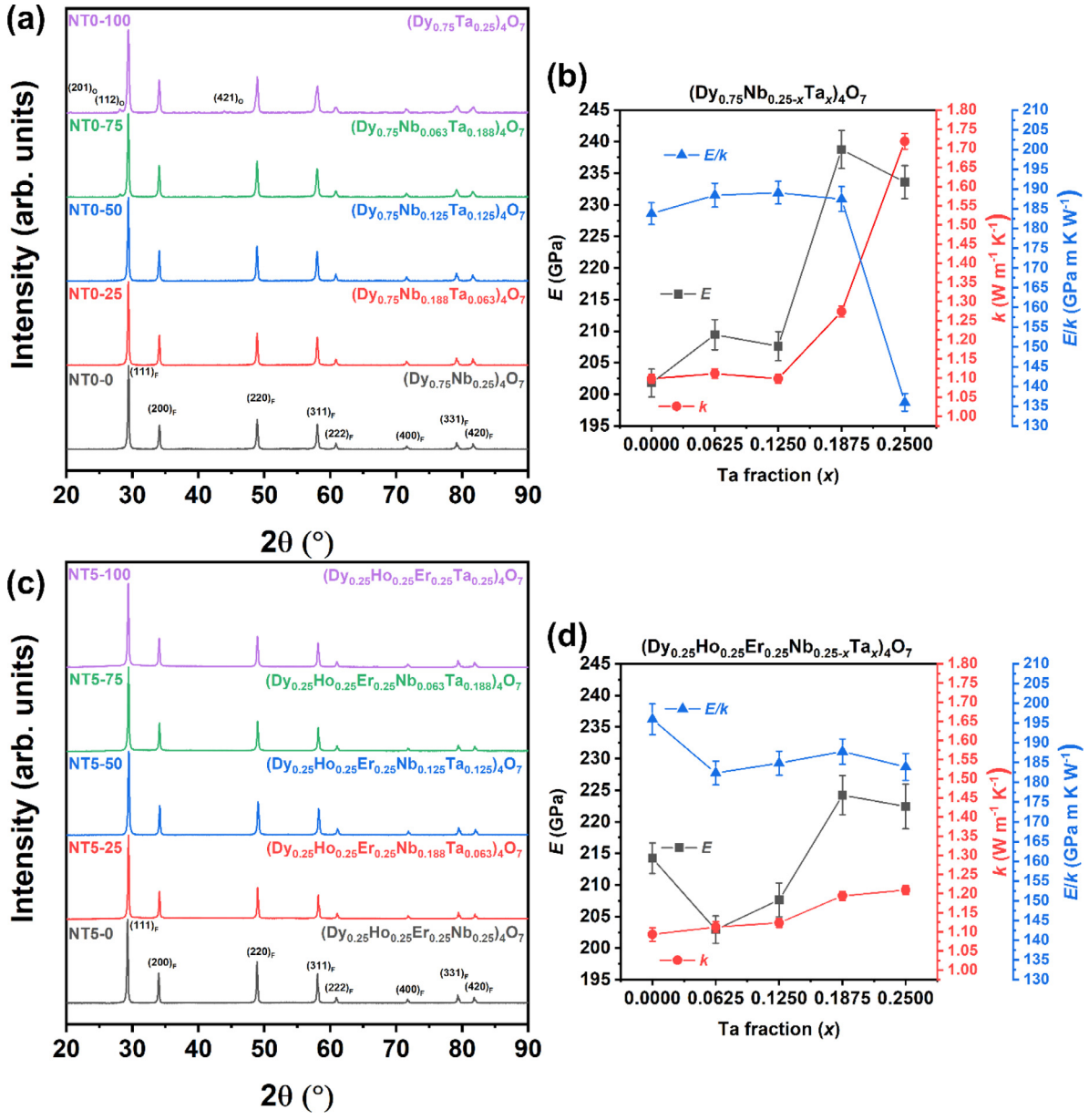

Fig. 1. **(a)** XRD pattern evolution from fluorite Dy_3NbO_7 to orthorhombic Dy_3TaO_7. **(b)** The Young's modulus (E), thermal conductivity (k), and E/k ratio for $Dy_3Nb_{1-x}Ta_xO7$ series. **(c)** XRD patterns and **(d)** the measured Young's modulus (E), thermal conductivity (k), and E/k ratio of a $(Dy_{0.25}Er_{0.25}Ho_{0.25}Nb_{0.25-x}Ta_x)_4O_7$ series.

Such elemental agglomeration may also have reduced the thermal conductivity.

3.4. Descriptor for thermal conductivity

The successful fabrication of 29 single-fluorite-phase niobates and tantalates enable us to conduct data-driven analysis to identify the controlling factors and the best descriptor. We first plotted the room temperature thermal conductivity k_{RT} *versus* six parameters ($\overline{r_{RE}^{3+}}/\overline{r_{Nb/Ta}^{5+}}$ ratio, size disorder δ_{size}, mass disorder g_{mass}, density ρ, and ideal mixing entropy $\Delta S^{mix,\ ideal}$, and average metal electronegativity $\bar{\chi}$) in Fig. 3(a) and Supplementary Fig. S1 and conducted correlation analyses to identify the controlling factors and the best descriptor. The correlations of the thermal conductivity measured at 1000 °C ($k_{1000\,^\circ C}$) with the same parameters are shown in Fig. 3(c) and Supplementary Fig. S2, which will be discussed further at the end of this section.

Previously, we showed that a size disorder parameter ($\delta_{size} = \sqrt{\sum_{i=0}^{n} x_i(1-r_{i/\bar{r}})^2}$, where x_i and r_i are the mole fraction and ionic radius of the ith component and $\bar{r}$ is the weighted average ionic radius) controls the reduced thermal conductivity in compositionally complex pyrochlore oxides ($\delta_{size} = \sqrt{(\delta_{size,\ A})^2 + (\delta_{size,\ B})^2}$ for $A_2B_2O_7$ pyrochlores with two cation sublattices) [26]. In that case, a strong negative correlation between δ_{size} and k_{RT} (*i.e.*, a larger δ_{size} implies a smaller k_{RT}) was also observed [26]. In the current case, a moderate negative correlation between δ_{size} and k_{RT} with a Pearson correlation coefficient (PCC) of −0.61 was observed for these compositionally complex niobates and tantalates (Supplementary Fig. S1(a)), which is consistent with the prior study [26]. It indicates that δ_{size} is still a (reasonably good) descriptor for forecasting reduced thermal conductivity, but it is less effective for compositionally complex niobates and tantalates than that for pyrochlore oxides [26].

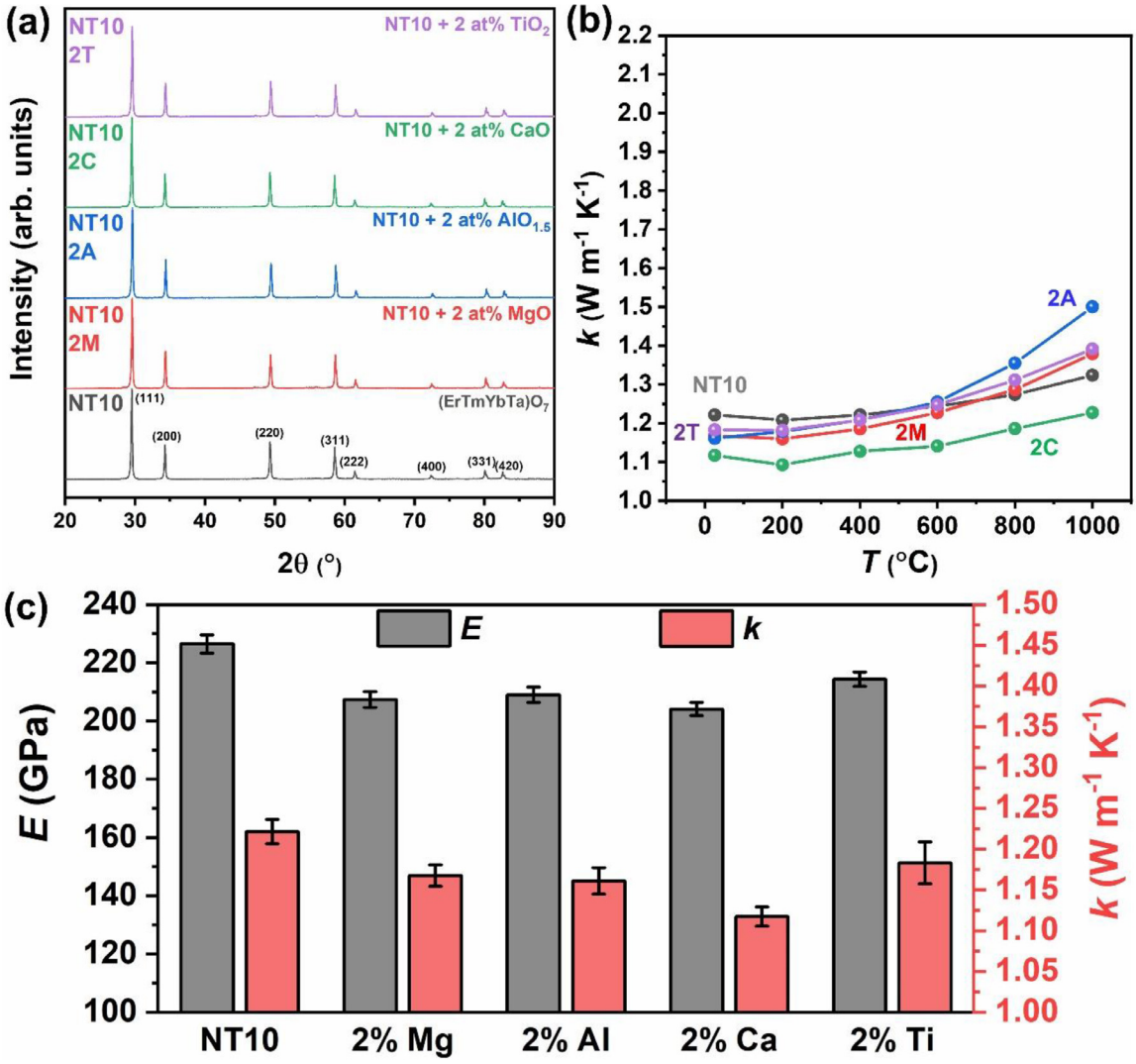

Fig. 2. **(a)** Benchtop XRD spectra and **(b)** temperature-dependent thermal conductivity of NT10, $(Er_{1/3}Tm_{1/3}Yb_{1/3})_3TaO_7$, doped with 2 mol.% MgO, $AlO_{1.5}$, CaO, and TiO_2. **(c)** Room temperature Young's modulus and thermal conductivity for each specimen. Note small satellite peaks, *e.g.*, those around 47° and 56°, were from W L_α contamination of the Cu target of the XRD unit used.

Instead, we observed a stronger negative correlation between $\overline{r_{RE}^{3+}}/\overline{r_{Nb/Ta}^{5+}}$ and k_{RT}, as shown in Fig. 3(a). Here, $\overline{r_{RE}^{3+}}$ is the weighted average effective ionic radius assuming a coordination number of VII according to Shannon [85] and $\overline{r_{Nb/Ta}^{5+}}$ is virtually a constant of 0.69 Å (since Nb^{5+} and Ta^{5+} have almost identical radii).

In addition, there is a rather complex relation between the mass disorder *vs.* k_{RT} (Supplementary Fig. S1(b)) that is not easily interpretable. Statistically, increased mass disorder leads to slightly increased thermal conductivity, which is counterintuitive. There is a weak negative correlation between k and density (PCC = −0.17, as shown in Supplementary Fig. S1(c)).

Notably, the reduced thermal conductivity is not due to the "high entropy" effect; in contrast, we observed a weak positive correlation between k and the ideal mixing entropy (PCC = 0.13, as shown in Supplementary Fig. S1(d)). This correlation indicates an increasing mixing entropy in fact leads to increased k_{RT} statistically (albeit that the correction is very weak and may not be statistically significant).

Although, electronegativity can correlate well with various properties due to its strong relationship to bond polarity, we only found a weak correlation between the thermal conductivity and the average metal electronegativity $\bar{\chi}$ (PCC = 0.25, as shown in Supplementary Fig. S1(e)).

In summary, $\overline{r_{RE}^{3+}}/\overline{r_{Nb/Ta}^{5+}}$ appears to be the most significant descriptor for forecasting k_{RT} in compositionally complex niobates and tantalates based on the 29 single-phase compositions obtained in this study. Fig. 3(a) shows that k_{RT} reduces with increasing $\overline{r_{RE}^{3+}}/\overline{r_{Nb/Ta}^{5+}}$, or the increasing average size of the rare-earth cations $\overline{r_{RE}^{3+}}$ (since $\overline{r_{Nb/Ta}^{5+}}$ = 0.69 Å, virtually independent of the Nb/Ta ratio).

This interesting finding may be correlated with ordering in RE_3NbO_7 and RE_3TaO_7, where it is known that larger RE cations form an ordered weberite-type phase while the smaller cations (*e.g.*, Dy in RE_3NbO_7 and Ho in RE_3TaO_7) form the disordered fluorite phase [5,87]. Fig. 3(b) expands Fig. 3(a) to include compositions from literature [73,84,88–90]. It shows that long-range ordered weberite-type phases form at high $\overline{r_{RE}^{3+}}/\overline{r_{Nb/Ta}^{5+}}$ ratios (>~1.43), but they exhibit high thermal conductivities.

Our data generally agrees with previous reports for the fluorite oxides. However, the data from literature are more scattered. Some reports, *e.g.*, Ref. [73] on a few ternary RE_3NbO_7 and a couple of high-entropy compounds, show surprisingly low thermal conduc-

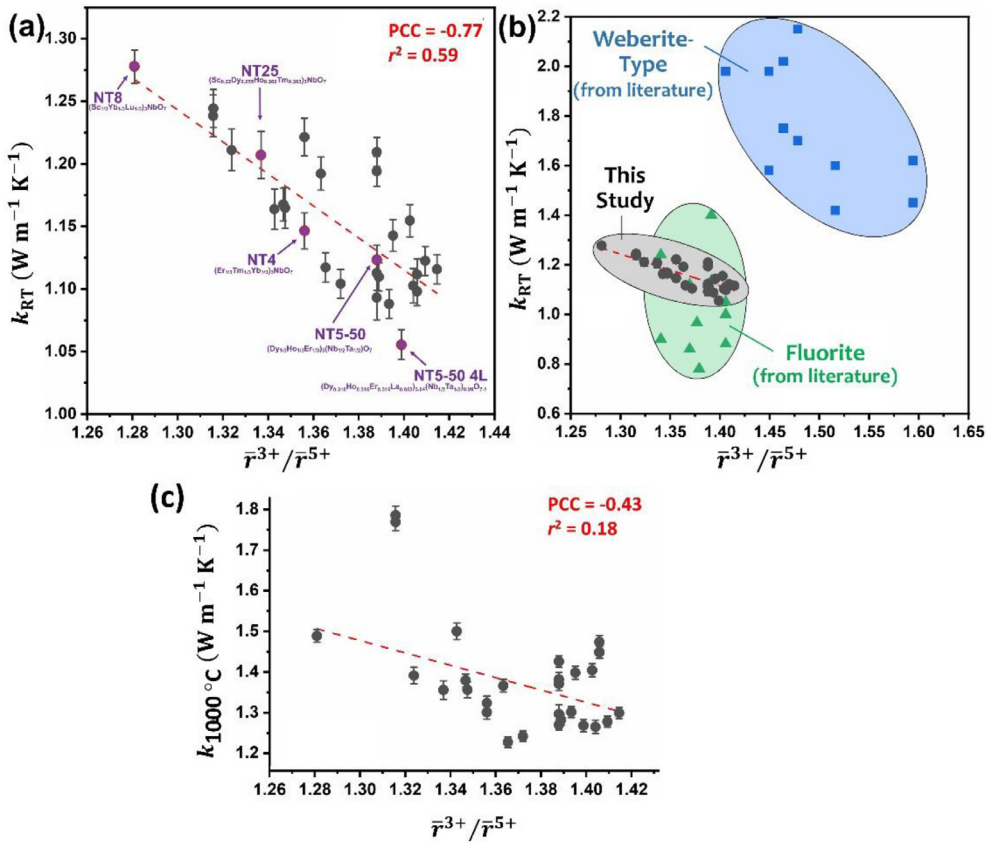

Fig. 3. **(a)** Correlation of room temperature thermal conductivity *vs.* the radius ratio of the 3+ cations to the 5+ cations. The highlighted specimens were selected for the neutron diffraction study. **(b)** Data in panel (a) expanded to include data of (long-range) fluorite and weberite-type structures from Refs. [73,84,88–90]. **(c)** Measured 1000 °C thermal conductivity *vs.* the radius ratio of the 3+ cations to the 5+ cations, showing a similar (albeit weaker) correlation.

tivities. These differences and scattered data are likely due to the differences in fabrications and measurements of thermal conductivities (*e.g.*, laser flash *vs.* hot-wire measurements), which can often have relatively large errors. In addition, the presence of residual porosity can often reduce the thermal conductivity appreciably. Thus, we mostly focus on comparing the relative values of our 29 single-phase compositions that were fabricated and measured via the same procedures, where we also carefully corrected the effects for porosity (so that all our data represent intrinsic thermal conductivities extrapolated for fully dense specimens).

The hypothesis that reducing thermal conductivity with increasing $\overline{r_{RE}^{3+}}/\overline{r_{Nb/Ta}^{5+}}$ is related to weberite-type order appears to be counterintuitive for the following two reasons. First, all the 29 single-phase compositionally complex niobates and tantalates are in the (at least nominally cubic) defect fluorite structure without long-range weberite-type ordering. Second, the long-range ordered (perfect) weberite-type phases typically have higher (instead of lower) thermal conductivities than defect fluorites. However, these apparently discrepancies can be fully explained and understood. We hypothesize that there is short-range weberite-type ordering in these compositionally complex niobates and tantalates, which maintain the long-range defect fluorite structure (nominally cubic based on XRD). Consequently, the formation of short-range orders, which have nanoscale characteristic size, can scatter phonons and reduce the thermal conductivity (in contrast to the increased thermal conductivity in the long-range ordered weberite-type phases).

Since RE niobates and tantalates with ultralow thermal conductivity have potential applications as TBCs, we further carried out correlation analyses for the thermal conductivities measured at 1000 °C, $k_{1000\,°C}$. Fig. 3(c) and Supplementary Fig. S2 show shows measured $k_{1000\,°C}$ *vs.* $\overline{r_{RE}^{3+}}/\overline{r_{Nb/Ta}^{5+}}$, size and mass disorder, theoretical density, ideal mixing configurational entropy, and average metal electronegativity. While similar trends were observed as the room temperature thermal conductivities k_{RT}, the correlations for the $k_{1000\,°C}$ measured at 1000°*C* with the same parameters are generally weaker. The measured $k_{1000°C}$ appears to have stronger correlations with the theoretical density, configurational entropy, and the average metal electronegativity (than those for k_{RT}), albeit still weak correlations. We note that thermal radiation becomes significant at $T > 600$ °C, which contribute to the scattered data (*i.e.*, measurement errors in $k_{1000°C}$ due to internal radiation, which depends on specimen composition and thickness that affect absorption).

To confirm and further analyze the existence of the short-range weberite-type ordering, we carried out XRD scattering and neutron diffraction on selective specimens. Five specimens labeled in Fig. 3(a), with representative k_{RT} and $\overline{r_{RE}^{3+}}/\overline{r_{Nb/Ta}^{5+}}$ values, were chosen for further in-depth study. These five selected compositions (labeled in Fig. 3(a)) are:

- NT8: $(Sc_{0.25}Yb_{0.25}Lu_{0.25}Nb_{0.25})_4O_7$, $\overline{r_{RE}^{3+}}/\overline{r_{Nb/Ta}^{5+}} = 1.218$; $k_{RT} = 1.28 \pm 0.04$ W m^{-1} K^{-1}
- NT25: $(Sc_{0.165}Dy_{0.191}Ho_{0.197}Tm_{0.197}Nb_{0.25})_4O_7$, $\overline{r_{RE}^{3+}}/\overline{r_{Nb/Ta}^{5+}} = 1.337$; $k_{RT} = 1.21 \pm 0.03$ W m^{-1} K^{-1}
- NT4: $(Er_{0.25}Tm_{0.25}Yb_{0.25}Nb_{0.25})_4O_7$, $\overline{r_{RE}^{3+}}/\overline{r_{Nb/Ta}^{5+}} = 1.356$; $k_{RT} = 1.15 \pm 0.04$ W m^{-1} K^{-1}
- NT5–50: $(Dy_{0.25}Ho_{0.25}Er_{0.25}Nb_{0.125}Ta_{0.125})_4O_7$, $\overline{r_{RE}^{3+}}/\overline{r_{Nb/Ta}^{5+}} = 1.388$; $k_{RT} = 1.12 \pm 0.01$ W m^{-1} K^{-1}
- NT5–50 4L: $(Sc_{0.25}Yb_{0.25}Lu_{0.25}Nb_{0.25})_4O_7$, $\overline{r_{RE}^{3+}}/\overline{r_{Nb/Ta}^{5+}} = 1.218$; $k_{RT} = 1.06 \pm 0.01$ W m^{-1} K^{-1}

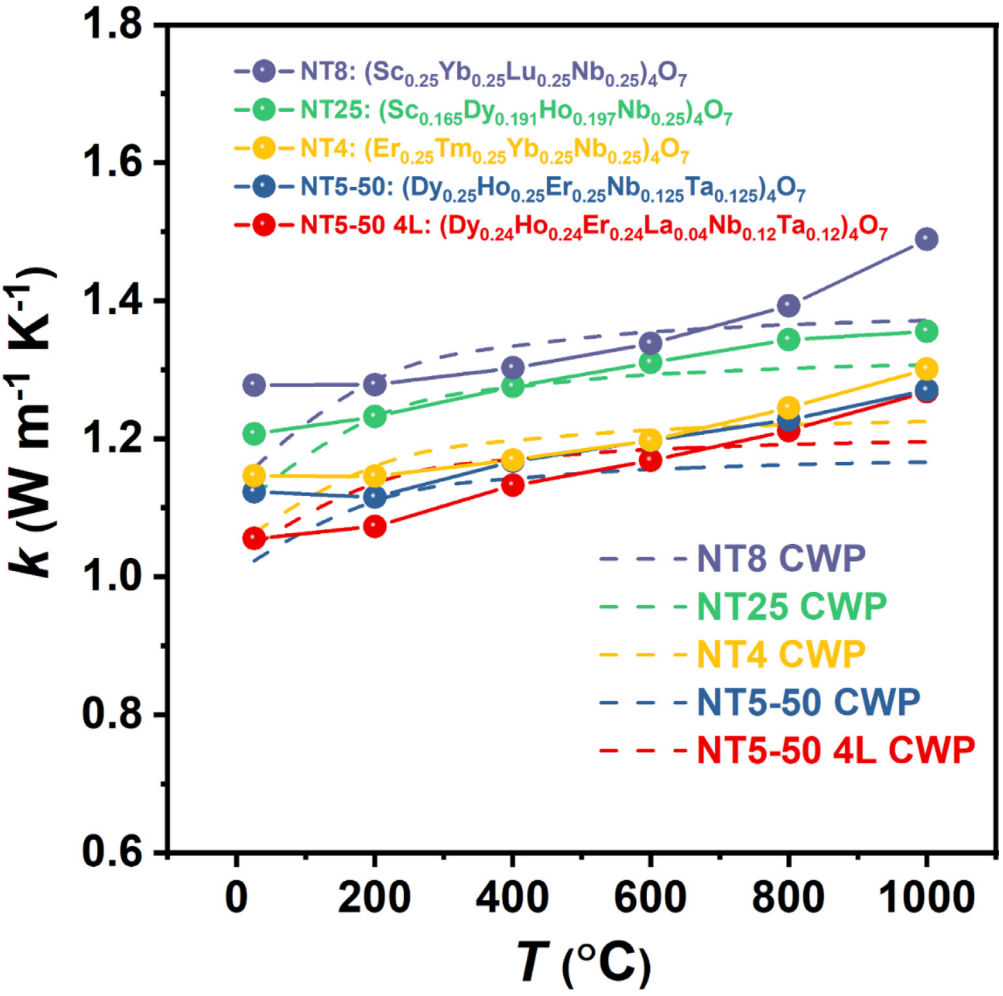

Fig. 4. Temperature-dependent thermal conductivity of the five selected specimens (NT8, NT25, NT4, NT5–50, and NT5–50 4L) from room temperature to 1000°C. The k_{min} as described by Cahill, Watson, and Pohl are shown as a dashed line [94].

3.5. Temperature-dependent thermal conductivity

Fig. 4 shows the thermal conductivities of five selected specimens up to 1000°C. Additional temperature-dependent thermal conductivities for all specimens are shown in Fig. 2(b) for 2% light element cation doped compositions and documented in Supplementary Figs. S5(b)–S13(b) for all other compositions.

All five selected compositionally complex RE niobates and tantalates show amorphous-like conductivity trends, where k increases slightly with temperature and plateaus at high temperatures (Fig. 4) [76,91–93]. Such a behavior has been noted in simpler compositions such as Dy_3NbO_7 and appears to be common in fluorite-structured niobates and tantalates [84]. The minimum thermal conductivity (k_{min}) was computed for each specimen according to the model developed by Cahill, Watson, and Pohl [94]. The phonon limit (k_{min}) occurs when the mean free path of the phonon approaches half the phonon wavelength (Ioffe-Regel limit) and it is usually prevalent in highly disordered materials (that are chemically, structurally, or electronically disordered) [76,95,96]. Fig. 4 shows that practically the thermal conductivities of all specimens lie below the k_{min} at intermediate temperatures (200 – 600 °C), while at high temperatures the thermal conductivity increases with temperature, possibly due to radiative contribution during laser flash measurements. Thermal conductivity lower than the k_{min} indicates significant diffuson-mediated thermal transport as opposed to the typical phonon transport where the thermal conductivity variation with temperature shows $1/T$ trend [98]. Agne et al. derived an expression for the diffuson limit, which lies significantly lower than the k_{min} derived by Cahill et al. [98]. Since the k_{RT} values for the selected compositions are similar to the ternary compositions with identical charge distribution, we propose that the ultralow thermal conductivity in compositionally complex compositions is also largely driven by structural disorder.

3.6. Long-range order vs. diffuse scattering in XRD and neutron diffraction

Benchtop XRD was carried out to determine the phase (long-range order). XRD patterns for five selected representative compositions are shown in Fig. 5(a) and additional XRD patterns for all compositions are documented in Supplementary Figs. S5(a)–S13(a).

The Bragg peaks in Fig. 5(a) correspond to a fluorite structure as expected. However, on closer inspection of the background, we noticed significant diffuse scattering occurring in all specimens around $2\theta = 40°$, 46°, and 55°, which, in general, is the hallmark of correlated disorder [97–99]. We have shown this in Fig. 5(b) on a logarithmic intensity scale for the five selected specimens with distinctly different conductivities and averaged RE cation radii. We also found that the magnitude of these broad peaks correlated with the measured k_{RT} (or the ratio of the average radii $\overline{r^{3+}_{RE}}/\overline{r^{5+}_{Nb/Ta}}$). Specifically, the smaller peaks were observed in compositions with lower conductivities and the more prevalent peaks were observed

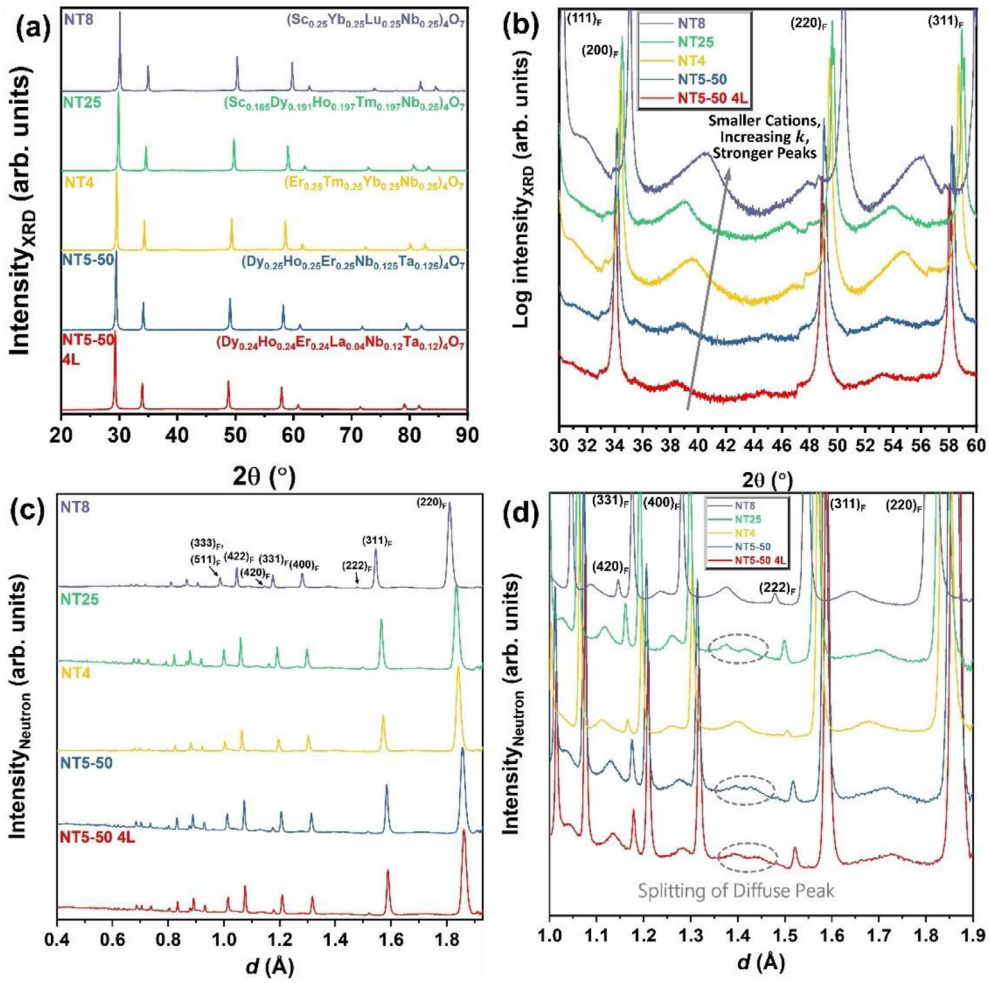

Fig. 5. Benchtop X-ray diffraction patterns of the five selected specimens on **(a)** a linear intensity scale and **(b)** a close-up of diffuse scattering present on a logarithmic intensity scale. **(c)** Neutron diffraction patterns (from the detector bank 4) of these five specimens and **(d)** the diffuse scattering around $d = 1.4$ Å in an expanded view.

those with higher conductivities. This correlation suggests that a smaller peak corresponds to a smaller weberite-type domain (so the peak is broadened into the background noises) on the nanometer scale, which leads to a stronger scattering of phonons by the nanodomains resulting in a lower thermal conductivity.

These same five specimens were further characterized by neutron diffraction. Neutron total scattering is more sensitive to oxygen compared to X-rays and makes it a great complement in diffraction studies. The intensity of the neutrons detected by bank 4 on NOMAD is provided in Fig. 5(c) and reveals more noticeable broad peaks in the background. A close-up of the background in Fig. 5(d) reveals these same broad diffuse scattering peaks with higher clarity. The same trend discerned from XRD is also noticed here when examining the same peaks, namely, more thermally insulative specimens have smaller diffuse peak intensities.

There is an additional feature in the neutron diffraction pattern that was not distinguishable in benchtop XRD. In all specimens, it was found that the frequently overlooked background contains rich information about diffuse scattering indicative of short-range ordering. Notably, there is a diffuse peak near 1.4 $Å^{-1}$ consists of two peaks in NT25, NT5–50, and NT5–50 4L (all containing Dy and Ho), whereas one broad peak exists in NT4 and NT8. This observation suggests that the materials with Dy and Ho have a stronger tendency for general short-range ordering, as evident by the increase in the number of peaks.

Similar diffuse scattering has been revealed by researchers in simpler rare-earth niobates and tantalates by Allpress and Rossell using electron diffraction patterns [100]. It was proposed then and confirmed later that the diffuse scattering corresponded to an orthorhombic weberite-type structure [75]. Thus, the observed diffuse scattering in both XRD and neutron diffraction for compositionally complex niobates and tantalates suggests the existence of short-range weberite-type ordering (on the nanoscale) albeit that these materials show a long-range disordered defect fluorite structure.

3.7. Scanning transmission electron microscopy

Aberration-corrected scanning transmission electron microscopy (AC STEM) high-angle annular dark field (HAADF) imaging was used to characterize NT5–50 ($(Dy_{0.25}Ho_{0.25}Er_{0.25}Nb_{0.125}Ta_{0.125})_4O_7$) as an example to probe the structural and compositional homogeneity at the atomic to nanometer scales. Fig. 6(a) shows the uniform composition (distribution of all cations) at the nanoscale for two grains across a grain boundary. Atomic-resolution STEM HAADF imaging further showed structural homogeneity at the atomic level, with a crystal structure that can be indexed to a fluorite structure, as shown in Fig. 6(b).

In brief, STEM and EDS show the compositional and structural homogeneity at the nanoscale and the atomic scale. We should

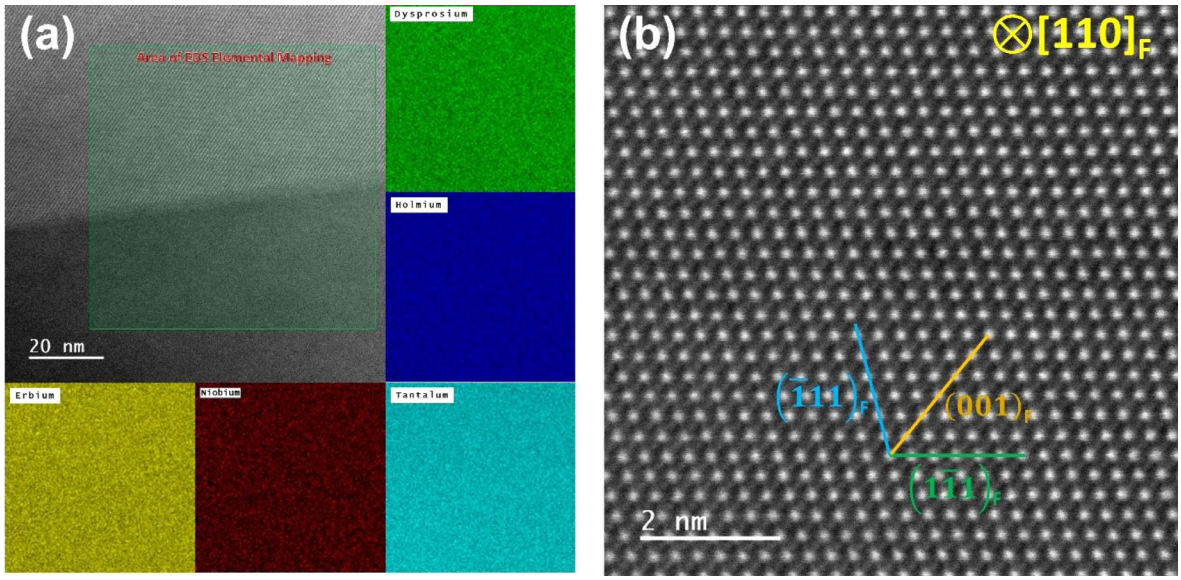

Fig. 6. **(a)** STEM image and EDS elemental maps of the NT5–50 specimen with a grain boundray, showing uniform elemental distribution at the nanoscale. **(b)** AC STEM HAADF image of the NT5–50 specimen, showing homogeneity at the atomic scale. Note that the weberite-type short-range ordering revealed by the diffuse peaks in the XRD and neutron total scattering, which is at a length scale of only ~1 nm based on the modeling of neutron total scattering, cannot be detected in STEM imaging that represents projected average intensities over the specimen thickness (> 50 nm).

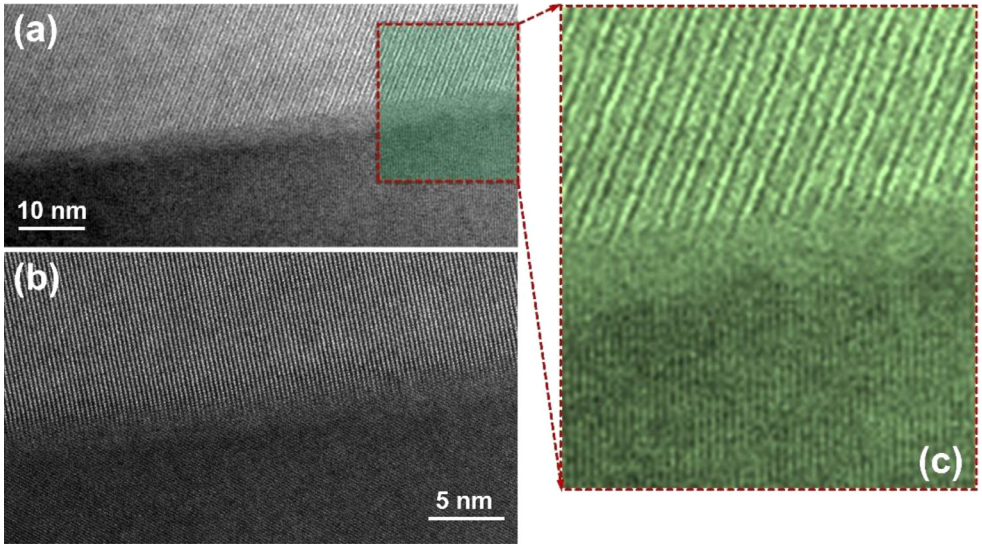

Fig. 7. Two high-magnification grain boundary images taken at different locations and along different zone axes of the same NT5–50 specimen **(a)** with and **(b)** without a nanometer-thick intergranular film. **(c)** An artificially colored image of a selected enlarged region of Panel (a) to highlight the amorphous-like intergranular film.

note that the subtle differences (in either the Z contrasts of different atom columns or the lattice parameters) between the defect fluorite and weberite-type structures may not be differentiated by STEM. However, we have carefully examined both XRD and neutron diffraction patterns (all the relevant sharp diffraction peaks) and found no peak splitting characteristic of orthorhombic long-range weberite order. Thus, we conclude that the long-range order is represented by the cubic fluorite. We further note that the weberite-type short-range order revealed by the diffuse peaks in XRD and the neutron total scattering, which is expected be at a length scale of only ~1 nm (0.5–1 nm) based on the modeling of neutron total scattering discussed later, cannot be detected in STEM imaging that represents projected averaged intensities over the specimen thickness (> 50 nm).

Fig. 7 shows two grain boundaries at different locations of the same NT5–50 specimen with and without the presence of a nanometer-thick intergranular film. An enlarged STEM image shown in Fig. 7(c) highlights the "amorphous-like" intergranular film. Such nanoscale amorphous-like 2D interfacial films [101,102] (albeit not fully amorphous) are known to form at grain boundaries in a variety of ceramics [101–104] and some metals [105–108], as well as on the surfaces of oxide ceramics [109–115]. They are known to promote sintering [101,103,104,106,107,116,117] and influence microstructural evolution [118–120]. They represent one type of most commonly known 2D interfacial phases, also named as "complexions" [118,119], at least in ceramics. This observation shown in Fig. 7(a) and 7(c) represents the first time such intergranular films (or "nanolayer" complexion [118]) are observed in high-entropy ceramics, albeit they do not form at all grain boundaries in the current case. The coexistence of two distinct grain boundray complexions ("amorphous-like" *vs.* "crystallize") may represent boundary-to-boundary variation (anisotropy that depends on the grain boundary character) [118] or the possible existence of interfacial complexion (phase-like) transitions [101,118,121–125].

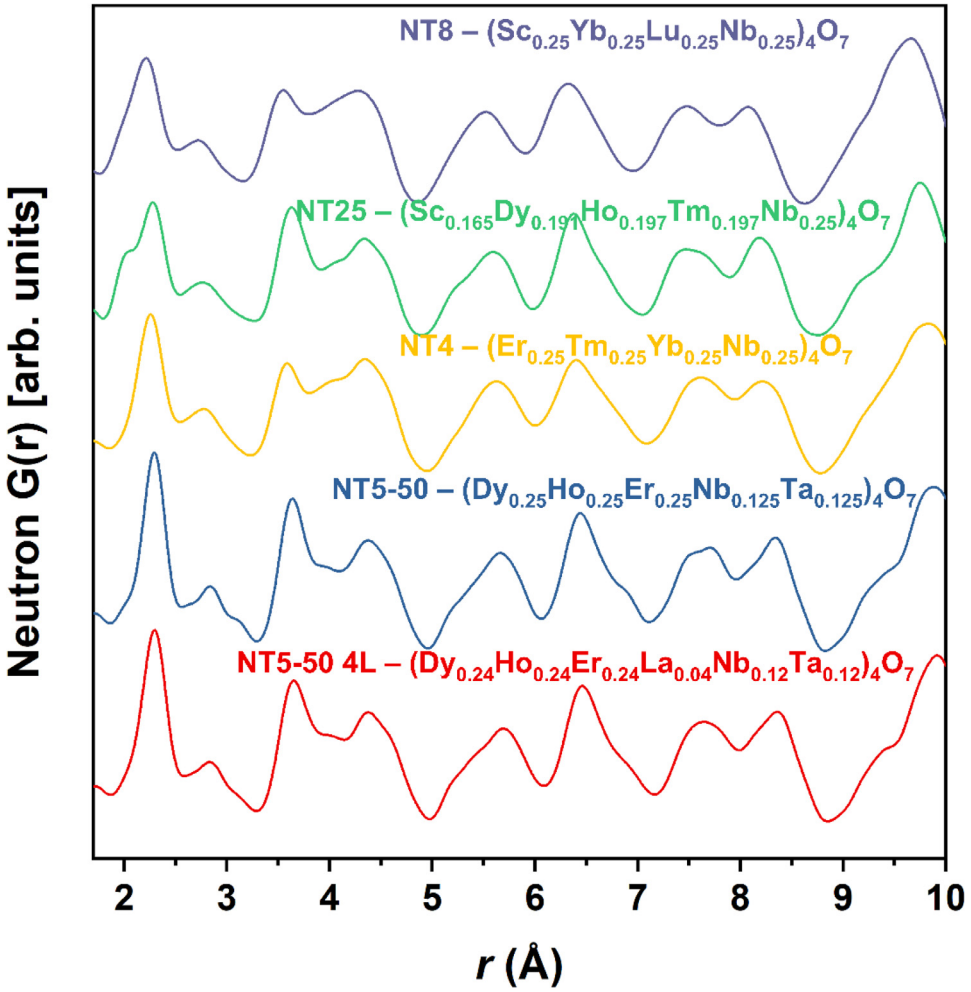

Fig. 8. The pair distribution functions (PDFs, $G(r)$) of the five selected specimens ($Q_{max} = 25$ Å^{-1}).

3.8. Short-range ordering indicated in neutron partial distribution function (PDF)

Various Q_{max} were used to analyze the the PDFs due to varying complexity of the compositions investigated regarding their neutron absorbing capabilities. examined as well. A couple were a sliding Q_{max} function that used a higher Q_{max} (45.4 Å^{-1} or 31.4 Å^{-1}) in the nearest neighbor interactions ($\sim$ 3 Å) and then transitioned to a lower Q_{max} (23 Å^{-1} and 18 Å^{-1}) as the radial distance increased. The purpose of the sliding Q_{max} was to increase the spatial resolution in the next nearest neighbor distances; however, this comes at the expense of higher statistical uncertainty. The pattern at the longer range distances is not as sharp as the nearest neighbor region so these were truncated earlier in reciprocal space without loss of intrinsic information. Another analysis used a fixed $Q_{max} = 25$ Å^{-1} and broadened it with a Lorch function. This reduces the statistical uncertainty in the nearest neighbor region, but the spatial resolution is then lost behind the broadening. Each of these analyses are in the Supplementary Material (Fig. S18). We opted to use a fixed $Q_{max} = 25$ Å^{-1} with no Lorch function as we found this to be the middle ground between uncertainty and resolution. Additionally, because of some strong neutron absorbers we have in our compositions (Dy and Ho), there are further uncertainties that arise when using a sliding Q_{max} function. Thus, all the data presented here was used with a fixed $Q_{max} = 25$ Å^{-1}.

Fig. 8 shows the PDF, $G(r)$, for all five specimens, which provides insight into the structure on the atomic scale in a histogram of the atom-atom distances. In general, each pattern had the same peaks and general shape alluding to the same general structure. On closer observation, it was found that the NT5–50 and NT5–50 4L specimens displayed slightly sharper peaks, especially around 2.8 Å. Specimen NT8, in particular, showed a very broad and convoluted pattern with little distinguishable fine features. This agrees with the consensus that the larger the size difference between the 3+ and 5+ cations, the higher the tendency for ordering. This is similar to the relationship between the pyrochlore and fluorite structure in rare-earth zirconates and hafnates [126–128]. Another difference is the slope in the 3.5 Å – 4 Å range is negative for NT5–50 and NT5–50 4L while it is positive for the other specimens suggesting this may be due to the presence of Ta.

Gussev et al. [129] and King et al. [75] are two previous cases that examined rare-earth tantalates and niobates with neutron total scattering methods. Qualitatively, the patterns are very similar and only display some differences in the nearest-neighbor region. For one, the Ta-O and Nb-O bond distances can be discerned while in the PDFs shown in this study, they are not too noticeable and are convoluted with the RE-O bonding peaks. This can be explained with a lower Q_{max} used in this study ($Q_{max} = 31.4$ Å^{-1} in Gussev et al.) and some smaller cations such as Lu^{3+} and Sc^{3+} used that become convoluted with the Nb-O and Ta-O peaks. Other qualitative differences arise from differences in neutron scattering

lengths. For example, the peak intensity ratio between the peaks at radial distance ~3.7 Å and ~4.5 Å. Overall, the PDFs are in good agreement and small differences come from the differences in chemistry and Q_{max} truncation.

We should note that Dy and Ho are strongly neutron absorbing elements, which may affect the accuracy of the PDFs of the samples that contain these elements. Specimens NT8 and NT4 likely have less of these uncertainties.

3.9. Small-box modeling with PDFgui

The PDFgui software was used to investigate the local structure and a possible transition between the fluorite and weberite-type structures. We approached this by first fitting the PDF to a fluorite and weberite-type structure over a large radial distance (50 Å). This was to provide general lattice parameters that serve as an average over a relatively large number of unit cells (~ 9 for the fluorite and ~ 6 for the weberite-type modeling). The maximum bound was decreased in 5 Å steps. This approached was followed to avoid any local minimums that may have resulted if this procedure was followed in reverse (*i.e.*, increasing the maximum bound from 10 Å in 5 Å steps). The R_w factor used to evaluate the fitting is given below:

$$R_w = \sum_{i=0}^{n} \left(\frac{w_i \left(Y_i^{obs} - Y_i^{calc}\right)^2}{\sum_{i=0}^{n} w_i \left(Y_i^{obs}\right)^2} \right)^{1/2} \times 100\% \quad (1)$$

Here, Y_i^{obs} and Y_i^{calc} were the experimental and calculated data and w_i is a weighting factor, which was set to unity. Additionally, the percent difference between the fluorite and weberite-type fitting factors were evaluated as a function of the fitting window.

Fig. 9(a–e) shows the R_w factor for the weberite-type and fluorite cells for each specimen. Across all materials, the weberite-type structure always produces lower R_w at all observed fitting windows. This is likely due to two reasons. First, the weberite-type structure has been found to be a better fit for fluorite in the tantalate fluorite structure previously in short fitting windows [75]. Second, there are more degrees of freedom in the weberite-type structure so that it is easier to achieve smaller R_w. Nonetheless, they tend to approach each other at sufficiently high radial distances. We focus on examining the trends in the change of R_w values as functions of $r_{\max}$ (instead of the absolute values of R_w for fitting fluorite *vs*. weberite-type structures) since this provides more insight.

While the weberite-type structure always produces smaller R_w than the fluorite structure for all cases (as discussed above), we focus on analyzing how the change of the relative value with changing $r_{\max}$. In NT8 (Fig. 9(a)), the difference (*i.e.*, the preference to fit weberite-type structure over fluorite) increases sharply with reducing $r_{\max}$. As the average size of the 3+ cations (or $\overline{r_{RE}^{3+}}/\overline{r_{Nb/Ta}^{5+}}$) increases, the fitting for the weberite-type cell becomes slightly worse (with a decrease in R_w for fitting the weberite-type structure, whereas an increase in R_w for fitting the fluorite structure) at small radial distances ($r_{\max} = 10$ Å) and the difference between the two structures becomes smaller with increasing $r_{\max}$. While the weberite-type cell is certainly preferred for NT5–50 and NT5–50 4L, the fit achieved is not as good as the other three specimens. We speculate that the weberite-type structure in NT5–50 and NT5–50 4L are distorted to a greater degree (than the others) due to the increased size mismatch, which in turn, provides a lower thermal conductivity. This is not upheld in NT5–50 4L since this specimen has a better fit for the weberite-type structure compared to NT5–50, although it has a larger $\overline{r_{RE}^{3+}}/\overline{r_{Nb/Ta}^{5+}}$. However, this may be due to the addition of La into the structure, making the rare-earth niobate/tantalate non-stoichiometric (RE^{3+}:(Nb, Ta)$^{5+}$ ≠ 3:1). This deviation from stoichiometry likely creates oxygen vacancies and promotes anti-site mixing that is not captured in PDFgui, thereby resulting in more disordering than expected.

Overall, we conclude that weberite-type (short-range) order becomes the more preferred structure at the small length scale of ~ 10 Å. This preference is slightly more pronounced in specimens with small average RE cation radii (or small $\overline{r_{RE}^{3+}}/\overline{r_{Nb/Ta}^{5+}}$) that has a loose correlation with reduced thermal conductivity (Fig. 9). In other words, this analysis suggests the occurrence of stronger short-range weberite-type ordering at the length scale of ~ 10 Å in compositions with smaller $\overline{r_{RE}^{3+}}/\overline{r_{Nb/Ta}^{5+}}$, which leads to higher thermal conductivity. Other crucial factors such as neutron absorption and scattering length/efficiencies along with using all-in-same atomic site for atomic displacement parameters with multicomponent compositions all play a large role in the results of this section as well. In addition to having a small sample size of five, a strong trend is not easily discernable. The approach to the fluorite curve is also slower for NT5–50 and NT5–50 4L suggesting a larger weberite-type domain size. This larger domain and "diffuse" (not sharp) boundary further complicates the short-range order weberite-type to long-range order fluorite boundary and plays a role in the lower thermal conductivity. Overall, these RE niobates and tantalates all exhibit ultralow thermal conductivity, which may be attributed to the weberite-type short-range ordering that transitions to the long-range fluorite order.

The percent difference between the fluorite and weberite-type fitting are shown in Fig. 9(f–j). These plots further assist in showing the relative preference for weberite-type short-range ordering in materials with smaller rare-earth cations at small radial distances and a slower approach to the fluorite fit. Again, we note that we focus on examining the trends in relative values as a function of $r_{\max}$, but not the absolute values, for the rationale as discussed above). There is no strict cutoff (the relative values of fitted R_w) for the weberite-type-to-fluorite transition. If we take a somewhat arbitrary 40% cutoff in Fig. 9(f–j), nanodomain sizes are likely only ~15–50 Å in most cases (Fig. 9(f–j)), and the nanodomain (or nanoscale ordering) becomes larger and more "diffuse" with reducing $\overline{r_{RE}^{3+}}/\overline{r_{Nb/Ta}^{5+}}$ (Fig. 9(f)). Thus, they are not the traditional nanodomains (as the size is too small). Instead, the fluorite-structured RE_3NbO_7 and RE_3TaO_7 are the weberite-type structure at nearly the atomic scale, but the orthorhombic weberite-type cells are randomly distributed in three dimensions, which average out to a cubic cell at some characteristic length (corresponding to the proposed 40% cutoff), as proposed recently by researchers studying $Ho_2Zr_2O_7$ [9,126,127,130].

Using this definition (the proposed 40% cutoff), the "domain sizes" or characteristic lengths for the short-range weberite-type ordering for NT8, NT25, NT4, NT5–50, and NT5–50 4L are 24 Å, N/A, 41 Å, 11 Å and 14 Å (as rough estimates; noting that the absolute values of these characteristic lengths may not be accurate because of the arbitrary selection of 40% cutoff, but their relative values and scale offer useful information). This concept still applies to thermal conduction as the vibrational density of states generated by this local weberite-type domain will be different than the outside bulk fluorite domain and attribute to phonon scattering. The domain size in NT5–50 and NT5–50 4L approaches the distance of one weberite-type unit cell (~ 10.5 × ~ 7.5 × ~ 7.5), which is where the definition of a phonon is no longer applicable [76,96]. At the Ioffe-Regel limit (phonon mean free path ~ a), the heat transfer is better described by a diffuson model where heat is carried through a random-walk model. This provides evidence as to why the thermal conductivity approaches and lies below the lower limit described by the phonon picture. It is noted that the fluorite fitting for NT25 was slightly worse compared to the other specimens so the 40% cutoff was never reached within the exam-

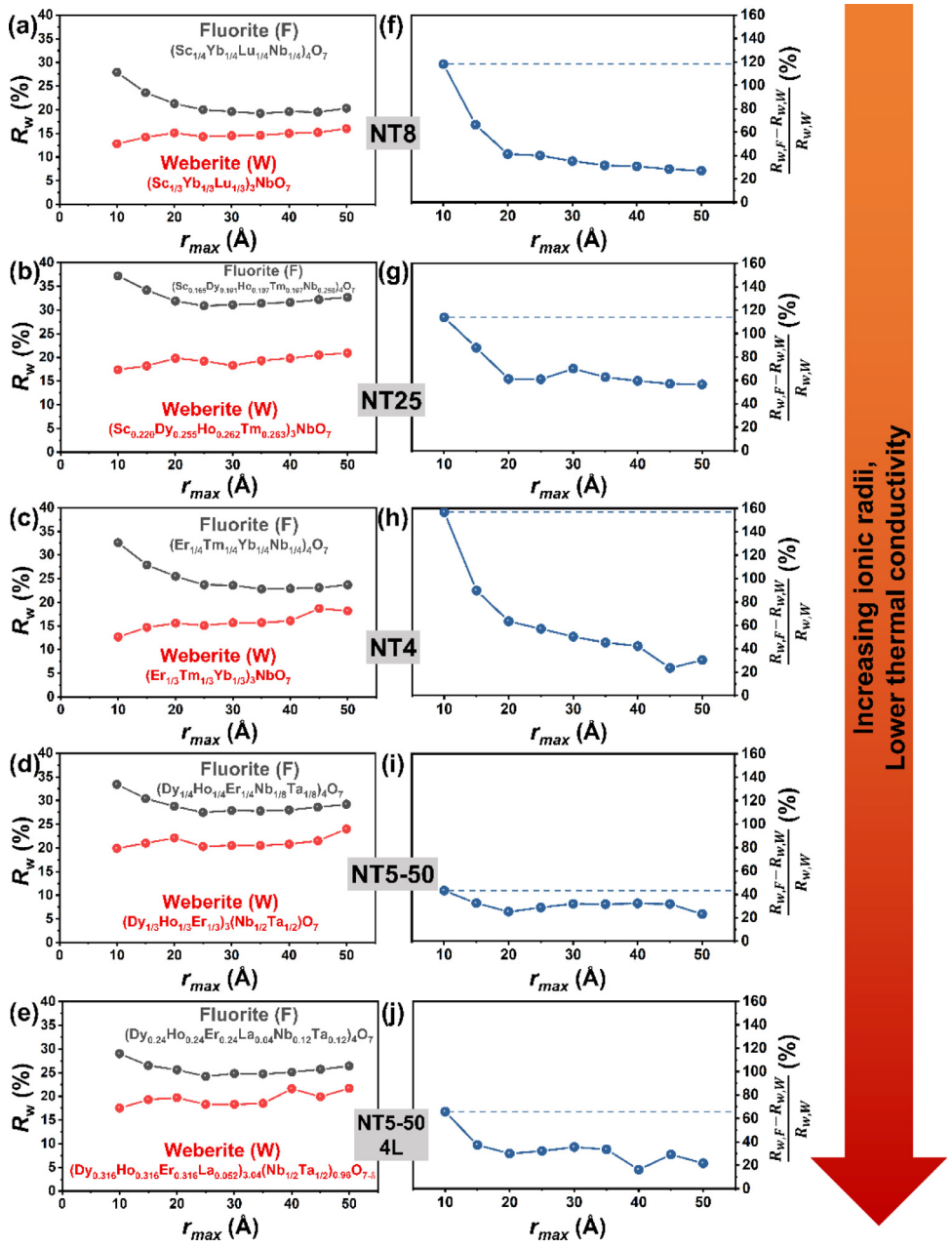

Fig. 9. **(a–e)** The fitting parameter R_w based on the upper bound of the fitting window for both the fluorite and weberite-type structures. The fitting began from 0.02 – 50Å and then was decreased in 5 Å steps to 0.02 – 10Å. After each step, the converged parameters from the previous step were used as the initial guess. **(f–j)** Percent difference between the fluorite and weberite-type R_w factors.

ined radial distances. No trend can be discerned from these five specimens likely because the dataset is small and the other factors such as the differing concentration of neutron absorbers affects the analysis. This again shows that it is unlikely to find one parameter to perfectly predict thermal conduction in these complex materials and other established phenomenon are still important. Here, we believe that NT25 lies outside the norm because it contains *Sc*. Scandium is a very light element and can transfer heat very efficiently due to high vibrational frequency it can achieve. In fact, all the compositions that contained *Sc* had the highest thermal conductivities among the niobates as shown in Table 1. Additional effects such as anti-site defects and oxygen vacancies likely play a role in the reduced conductivity of NT5–50 4L, although it has a larger predicted domain size than NT5–50.

Moreover, we should note that the amorphous limit may be different for different compositions (*e.g.*, higher in NT25). Thus, how the thermal conductivity is compared to the amorphous limit is more important than the absolute thermal conductivity, in term of understanding the underlying physics.

An example of the fluorite and weberite-type fitting NT4 to a 10 Å limit using PDFgui is shown in Fig. 10. The fluorite model is unable to capture peaks around 2.7 Å (Fig. 10(a)). The resulting R_w was 32.6%. The weberite-type model improves this to 12.7% (Fig. 10(b)) by capturing the general feature of nearest-neighbor region, yet some details are still missed. Additionally, some features are likely hidden behind the broadening and are not modeled properly since the actual pair-distribution functions are sharper than what appears here. However, as we increase Q_{max} and thereby

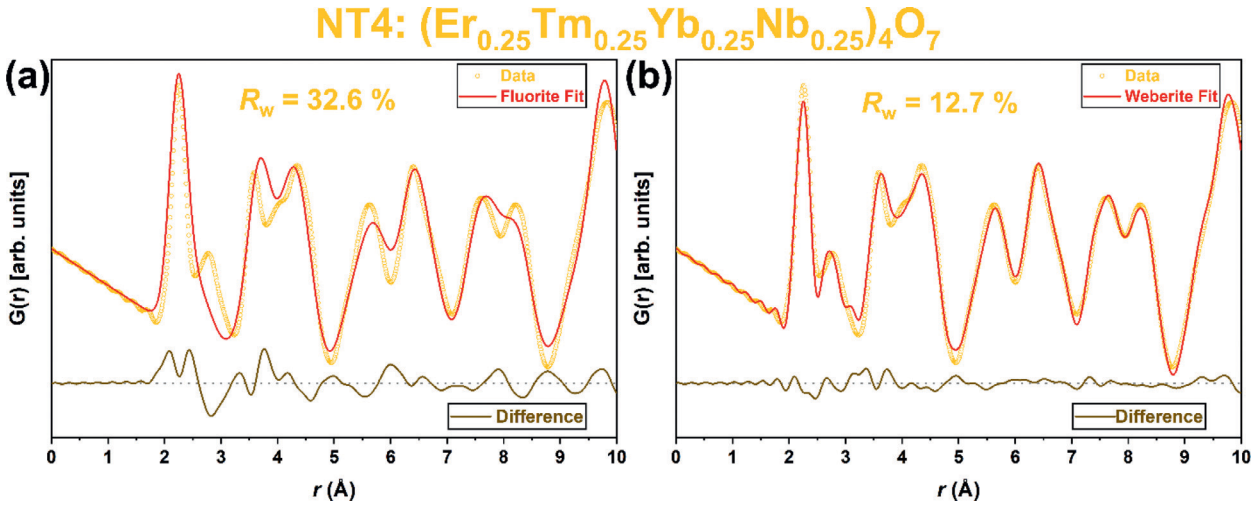

Fig. 10. The fitting and difference curve of the NT4 specimen up to 10 Å based on the **(a)** fluorite *vs.* **(b)** weberite-type structure using the PDFgui software.

the spatial resolution, we are unable to tell if certain features or peaks are artifacts or not. PDFgui, in general, is a very simplified approach since it uses average parameters for a unit cell to model data. This has strong limitations in simple ternary niobates/tantalates such as Yb_3TaO_7 [75]. This is expected to be exacerbated as the complexity of the composition increases, thereby requiring the use of more in-depth simulations and other experimental techniques to validate conclusions. In particular, the atomic site-sharing and atomic displacement parameters were approached in a simplified manner to reduce our degrees of freedom and uncertainties. Doing so, however, likely affects our results and limits our conclusions.

Our key finding here is that the weberite-type structure exists on the atomic scale (short-range order) in all the RE niobates and tantalates that show a long-range fluorite structure. In fact, from the few cases that we examined, the specimens with the least distinguishable features (*e.g.*, NT8 and NT4) displayed the strongest weberite-type structure on the nearest-neighbor scale. In other specimens such as NT5–50 and NT5–50 4L, the weberite-type to fluorite changes appears to be more gradual. These results are merely speculation into how these affect the thermal properties since there are many factors at play. However, the radius ratio, $\overline{r_{RE}^{3+}}/\overline{r_{Nb/Ta}^{5+}}$, appears to be a suitable descriptor that possibly accounts for all of these effects in a simple approximation. This is similar to how the radius ratio describing the fluorite-to-pyrochlore transition, r_A^{3+}/r_B^{4+}, embodies the complex phenomenon of anti-site mixing energetics [128]. Inelastic neutron scattering experiments are proposed to obtain the phonon dispersion curves to see how the observed correlated disorder *versus* random disorder affects phonon broadening.

4. Conclusions

Overall, 40 RE niobates and tantalates, including 29 single-phase defect fluorite compositions, were synthesized to advance the understanding of this emerging class of low thermal conductivity materials. Based on this rather large set of data, we found that the average size of the 3+ RE cations (or $\overline{r_{RE}^{3+}}/\overline{r_{Nb/Ta}^{5+}}$ cation radii ratio) is a good descriptor to forecast trends in room-temperature thermal conductivity.

Five selected representative compositions were chosen for further in-depth characterizations. The temperature-dependent thermal conductivity confirms the glass-like trend with value approaching or slightly falling below the phonon limit. XRD revealed a long-range order fluorite structure but indicated diffuse scattering peaks representative of the orthorhombic weberite-type structure in the background. Neutron diffraction increased the clarity of these diffuse scattering peaks. The neutron PDFs showed the lowest thermal conductivity specimens (which had the largest cations) exhibited more short-range weberite-type ordering. A small-box modeling approach on these PDFs reveal the lower thermal conductivity materials generally fit stronger to a weberite-type structure in the nearest-neighbor region compared to the fluorite structure, but appear to have a gradual transition from short-range to long-range order. This finding is consistent with a small weberite-type domain size approaching the Ioffe-Regel limit (*i.e.*, phonon limit). While the structure is correlated on the presence of certain elements, it does not correlate well with the thermal conductivity. Instead, it is suggested that a simple descriptor, $\overline{r_{RE}^{3+}}/\overline{r_{Nb/Ta}^{5+}}$, may embody various factors into a simple parameter to forecast trends in reduced thermal conductivity in this class of materials.

We also revealed that doping of small amount of light element oxides can further reduce the room temperature thermal conductivity of single-phase high-entropy tantalates (and potentially also niobates) studied here, which suggests another route to further tailor the thermomechanical properties of compositionally complex RE niobates and tantalates via incorporating “nonconventional” dopants.

Declaration of Competing Interest

The authors declare that they have no known competing financial interests or personal relationships that could have appeared to influence the work reported in this paper.

Acknowledgement

This project on the fundamental research of the role of disorder and short-range ordering in influencing thermomechanical properties, including the neutron total scattering analysis of short-range ordering and its role in reduced thermal conductivity, is supported by the National Science Foundation (NSF) via Grant No. DMR-2026193 since August 2020. We also acknowledge a prior seed (Small Innovative Projects in Solar) project supported by the U.S. DOE Solar Energy Technologies Office, where some materials were fabricated and thermal conductivities were measured before August 2020 in an effort to develop new low thermal conductivity

coatings for concentrated solar power (CSP) applications. A portion of this research used resources at the Spallation Neutron Source, a DOE Office of Science User Facility operated by the Oak Ridge National Laboratory.

Supplementary materials

Supplementary material associated with this article can be found, in the online version, at doi:10.1016/j.actamat.2022.118056.

References

[1] L. Lõpez-Conesa, J.M. Rebled, M.H. Chambrier, K. Boulahya, J.M. González-Calbet, M.D. Braida, G. Dezanneau, S. Estradé, F. Peirõ, Local structure of rare earth niobates (RE3NbO7, RE = Y, Er, Yb, Lu) for proton conduction applications, Fuel Cells 13 (2013) 29–33, doi:10.1002/fuce.201200136.

[2] H.P. Rooksby, E.A.D. White, Rare-earth niobates and tantalates of defect fluorite- and weberite-type structures, J. Am. Ceram. Soc. 47 (1964) 94–96, doi:10.1111/j.1151-2916.1964.tb15663.x.

[3] A. Mielewczyk-Gryn, A. Navrotsky, Enthalpies of formation of rare earth niobates, RE3NbO7, Am. Mineral. 100 (2015) 1578–1583, doi:10.2138/am-2015-5210.

[4] K.P.F. Siqueira, J.C. Soares, E. Granado, E.M. Bittar, A.M. De Paula, R.L. Moreira, A. Dias, Synchrotron X-ray diffraction and Raman spectroscopy of Ln3NbO7 (Ln=La, Pr, Nd, Sm-Lu) ceramics obtained by molten-salt synthesis, J. Solid State Chem. 209 (2014) 63–68, doi:10.1016/j.jssc.2013.10.015.

[5] M. Wakeshima, H. Nishimine, Y. Hinatsu, Crystal structures and magnetic properties of rare earth tantalates RE3TaO7 (*Re* = rare earths), J. Phys. Condens. Matter. 16 (2004) 4103–4120, doi:10.1088/0953-8984/16/23/025.

[6] Y. Hinatsu, Y. Doi, Studies on phase transitions of rare earth tantalates (Sm1-xLnx)3TaO7 (Ln = Nd, Eu) with fluorite-related structure, J. Ceram. Soc. Jpn. 127 (2019) 273–278, doi:10.2109/jcersj2.18219.

[7] N.P. Padture, M. Gell, E.H. Jordan, Thermal barrier coatings for gas-turbine engine applications, Science 296 (2002) 280–284 80-., doi:10.1126/science.1068609.

[8] N.P. Padture, Advanced structural ceramics in aerospace propulsion, Nat. Mater. 15 (2016) 804–809, doi:10.1038/nmat4687.

[9] J. Shamblin, C.L. Tracy, R.I. Palomares, E.C. O'Quinn, R.C. Ewing, J. Neuefeind, M. Feygenson, J. Behrens, C. Trautmann, M. Lang, Similar local order in disordered fluorite and aperiodic pyrochlore structures, Acta Mater. 144 (2018) 60–67, doi:10.1016/j.actamat.2017.10.044.

[10] A.J. Wright, J. Luo, A step forward from high-entropy ceramics to compositionally complex ceramics: a new perspective, J. Mater. Sci. (2020) 1–16, doi:10.1007/s10853-020-04583-w.

[11] R.Z. Zhang, M.J. Reece, Review of high entropy ceramics: design, synthesis, structure and properties, J. Mater. Chem. A 7 (2019) 22148–22162, doi:10.1039/C9TA05698J.

[12] A. Sarkar, Q. Wang, A. Schiele, M.R. Chellali, S.S. Bhattacharya, D. Wang, T. Brezesinski, H. Hahn, L. Velasco, B. Breitung, High-entropy oxides: fundamental aspects and electrochemical properties, Adv. Mater. 31 (2019) 1806236, doi:10.1002/adma.201806236.

[13] C.M. Rost, Z. Rak, D.W. Brenner, J.P. Maria, Local structure of the MgxNixCoxCuxZnxO(x=0.2) entropy-stabilized oxide: an EXAFS study, J. Am. Ceram. Soc. 100 (2017) 2732–2738, doi:10.1111/jace.14756.

[14] C.M. Rost, E. Sachet, T. Borman, A. Moballegh, E.C. Dickey, D. Hou, J.L. Jones, S. Curtarolo, J.P. Maria, Entropy-stabilized oxides, Nat. Commun. 6 (2015) 1–8, doi:10.1038/ncomms9485.

[15] D. Bérardan, S. Franger, D. Dragoe, A.K. Meena, N. Dragoe, Colossal dielectric constant in high entropy oxides, Phys. Status Solidi Rapid Res. Lett. 10 (2016) 328–333, doi:10.1002/pssr.201600043.

[16] S. Jiang, T. Hu, J. Gild, N. Zhou, J. Nie, M. Qin, T. Harrington, K. Vecchio, J. Luo, A new class of high-entropy perovskite oxides, Scr. Mater. 142 (2018) 116–120, doi:10.1016/j.scriptamat.2017.08.040.

[17] D.A. Vinnik, E.A. Trofimov, V.E. Zhivulin, S.A. Gudkova, O.V. Zaitseva, D.A. Zherebtsov, A.Y. Starikov, D.P. Sherstyuk, A.A. Amirov, A.V. Kalgin, S.V. Trukhanov, F.V. Podgornov, High entropy oxide phases with perovskite structure, Nanomaterials 10 (2020) 268, doi:10.3390/nano10020268.

[18] F. Okejiri, Z. Zhang, J. Liu, M. Liu, S. Yang, S. Dai, Room-temperature synthesis of high-entropy perovskite oxide nanoparticle catalysts through ultrasonication-based method, ChemSusChem (2020), doi:10.1002/cssc.201902705.

[19] Y. Sharma, B.L. Musico, X. Gao, C. Hua, A.F. May, A. Herklotz, A. Rastogi, D. Mandrus, J. Yan, H.N. Lee, M.F. Chisholm, V. Keppens, T. Zac Ward, Single-crystal high entropy perovskite oxide epitaxial films, Phys. Rev. Mater. 2 (2018), doi:10.1103/PhysRevMaterials.2.060404.

[20] K. Chen, X. Pei, L. Tang, H. Cheng, Z. Li, C. Li, X. Zhang, L. An, A five-component entropy-stabilized fluorite oxide, J. Eur. Ceram. Soc. 38 (2018) 4161–4164, doi:10.1016/j.jeurceramsoc.2018.04.063.

[21] J. Gild, M. Samiee, J.L. Braun, T. Harrington, H. Vega, P.E. Hopkins, K. Vecchio, J. Luo, High-entropy fluorite oxides, J. Eur. Ceram. Soc. 38 (2018) 3578–3584, doi:10.1016/j.jeurceramsoc.2018.04.010.

[22] A.J. Wright, Q. Wang, C. Huang, A. Nieto, R. Chen, J. Luo, From high-entropy ceramics to compositionally-complex ceramics: a case study of fluorite oxides, J. Eur. Ceram. Soc. 40 (2020) 2120–2129, doi:10.1016/j.jeurceramsoc.2020.01.015.

[23] Z. Zhao, H. Chen, H. Xiang, F.Z. Dai, X. Wang, W. Xu, K. Sun, Z. Peng, Y. Zhou, High entropy defective fluorite structured rare-earth niobates and tantalates for thermal barrier applications, J. Adv. Ceram. 9 (2020) 303–311, doi:10.1007/s40145-020-0368-7.

[24] R. Djenadic, A. Sarkar, O. Clemens, C. Loho, M. Botros, V.S.K. Chakravadhanula, C. Kübel, S.S. Bhattacharya, A.S. Gandhi, H. Hahn, Multicomponent equiatomic rare earth oxides, Mater. Res. Lett. 5 (2017) 102–109, doi:10.1080/21663831.2016.1220433.

[25] A. Sarkar, C. Loho, L. Velasco, T. Thomas, S.S. Bhattacharya, H. Hahn, R. Djenadic, Multicomponent equiatomic rare earth oxides with a narrow band gap and associated praseodymium multivalency, Dalton Trans. 46 (2017) 12167–12176, doi:10.1039/c7dt02077e.

[26] A.J. Wright, Q. Wang, S.T. Ko, K.M. Chung, R. Chen, J. Luo, Size disorder as a descriptor for predicting reduced thermal conductivity in medium- and high-entropy pyrochlore oxides, Scr. Mater. 181 (2020) 76–81, doi:10.1016/j.scriptamat.2020.02.011.

[27] F. Li, L. Zhou, J.X. Liu, Y. Liang, G.J. Zhang, High-entropy pyrochlores with low thermal conductivity for thermal barrier coating materials, J. Adv. Ceram. 8 (2019) 576–582, doi:10.1007/s40145-019-0342-4.

[28] Z. Teng, L. Zhu, Y. Tan, S. Zeng, Y. Xia, Y. Wang, H. Zhang, Synthesis and structures of high-entropy pyrochlore oxides, J. Eur. Ceram. Soc. (2019), doi:10.1016/j.eplepsyres.2019.106192.

[29] J. Gild, Y. Zhang, T. Harrington, S. Jiang, T. Hu, M.C. Quinn, W.M. Mellor, N. Zhou, K. Vecchio, J. Luo, High-entropy metal diborides: a new class of high-entropy materials and a new type of ultrahigh temperature ceramics, Sci. Rep. 6 (2016) 37946, doi:10.1038/srep37946.

[30] Y. Zhang, Z. Bin Jiang, S.K. Sun, W.M. Guo, Q.S. Chen, J.X. Qiu, K. Plucknett, H.T. Lin, Microstructure and mechanical properties of high-entropy borides derived from boro/carbothermal reduction, J. Eur. Ceram. Soc. 39 (2019) 3920–3924, doi:10.1016/j.jeurceramsoc.2019.05.017.

[31] Y. Zhang, W.M. Guo, Z. Bin Jiang, Q.Q. Zhu, S.K. Sun, Y. You, K. Plucknett, H.T. Lin, Dense high-entropy boride ceramics with ultra-high hardness, Scr. Mater. 164 (2019) 135–139, doi:10.1016/j.scriptamat.2019.01.021.

[32] J. Gild, K. Kaufmann, K. Vecchio, J. Luo, Reactive flash spark plasma sintering of high-entropy ultrahigh temperature ceramics, Scr. Mater. 170 (2019) 106–110, doi:10.1016/j.scriptamat.2019.05.039.

[33] J. Zhou, J. Zhang, F. Zhang, B. Niu, L. Lei, W. Wang, High-entropy carbide: a novel class of multicomponent ceramics, Ceram. Int. 44 (2018) 22014–22018, doi:10.1016/j.ceramint.2018.08.100.

[34] X. Han, V. Girman, R. Sedlák, J. Dusza, E.G. Castle, Y. Wang, M. Reece, C. Zhang, Improved creep resistance of high entropy transition metal carbides, J. Eur. Ceram. Soc. (2019).

[35] T.J. Harrington, J. Gild, P. Sarker, C. Toher, C.M. Rost, O.F. Dippo, C. McElfresh, K. Kaufmann, E. Marin, L. Borowski, P.E. Hopkins, J. Luo, S. Curtarolo, D.W. Brenner, K.S. Vecchio, Phase stability and mechanical properties of novel high entropy transition metal carbides, Acta Mater 166 (2019) 271–280, doi:10.1016/j.actamat.2018.12.054.

[36] X. Yan, L. Constantin, Y. Lu, J.F. Silvain, M. Nastasi, B. Cui, (Hf0.2Zr0.2Ta0.2Nb0.2Ti0.2)C high-entropy ceramics with low thermal conductivity, J. Am. Ceram. Soc. 101 (2018) 4486–4491, doi:10.1111/jace.15779.

[37] E. Castle, T. Csanádi, S. Grasso, J. Dusza, M. Reece, Processing and properties of high-entropy ultra-high temperature carbides, Sci. Rep. 8 (2018) 8609, doi:10.1038/s41598-018-26827-1.

[38] M. Qin, Q. Yan, H. Wang, C. Hu, K.S. Vecchio, J. Luo, High-entropy monoborides: towards superhard materials, Scr. Mater. 189 (2020) 101–105, doi:10.1016/j.scriptamat.2020.08.018.

[39] M. Qin, Q. Yan, Y. Liu, J. Luo, A new class of high-entropy M 3 B 4 borides, J. Adv. Ceram. 10 (2021) 166–172, doi:10.1007/s40145-020-0438-x.

[40] M. Qin, Q. Yan, H. Wang, K.S. Vecchio, J. Luo, High-entropy rare earth tetraborides, J. Eur. Ceram. Soc. 41 (2021) 2968–2973, doi:10.1016/j.jeurceramsoc.2020.12.019.

[41] H. Chen, Z. Zhao, H. Xiang, F.Z. Dai, J. Zhang, S. Wang, J. Liu, Y. Zhou, Effect of reaction routes on the porosity and permeability of porous high entropy (Y0.2Yb0.2Sm0.2Nd0.2Eu0.2)B6 for transpiration cooling, J. Mater. Sci. Technol. 38 (2020) 80–85, doi:10.1016/j.jmst.2019.09.006.

[42] M. Qin, Q. Yan, Y. Liu, H. Wang, C. Wang, T. Lei, K.S. Vecchio, H.L. Xin, T.J. Rupert, J. Luo, Bulk high-entropy hexaborides, J. Eur. Ceram. Soc. 41 (2021) 5775–5781, doi:10.1016/j.jeurceramsoc.2021.05.027.

[43] J. Gild, J. Braun, K. Kaufmann, E. Marin, T. Harrington, P. Hopkins, K. Vecchio, J. Luo, A high-entropy silicide: (Mo0.2Nb0.2Ta0.2Ti0.2W0.2)Si2, J. Mater. 5 (2019) 337–343, doi:10.1016/j.jmat.2019.03.002.

[44] Y. Qin, J.X. Liu, F. Li, X. Wei, H. Wu, G.J. Zhang, A high entropy silicide by reactive spark plasma sintering, J. Adv. Ceram. 8 (2019) 148–152, doi:10.1007/s40145-019-0319-3.

[45] Y. Qin, J.C. Wang, J.X. Liu, X.F. Wei, F. Li, G.J. Zhang, C. Jing, J. Zhao, H. Wu, High-entropy silicide ceramics developed from (TiZrNbMoW)Si2 formulation doped with aluminum, J. Eur. Ceram. Soc. (2020), doi:10.1016/j.jeurceramsoc.2020.02.059.

[46] N. Zhou, S. Jiang, T. Huang, M. Qin, T. Hu, J. Luo, Single-phase high-entropy intermetallic compounds (HEICs): bridging high-entropy alloys and ceramics, Sci. Bull. 64 (2019) 856–864, doi:10.1016/j.scib.2019.05.007.

[47] D. Moskovskikh, S. Vorotilo, V. Buinevich, A. Sedegov, K. Kuskov, A. Khort, C. Shuck, M. Zhukovskyi, A. Mukasyan, Extremely hard and tough

high entropy nitride ceramics, Sci. Rep. 10 (2020) 1–8, doi:10.1038/s41598-020-76945-y.
[48] O.F. Dippo, N. Mesgarzadeh, T.J. Harrington, G.D. Schrader, K.S. Vecchio, Bulk high-entropy nitrides and carbonitrides, Sci. Rep. 10 (2020), doi:10.1038/s41598-020-78175-8.
[49] X. Chen, Y. Wu, High-entropy transparent fluoride laser ceramics, J. Am. Ceram. Soc. 103 (2019) 750–756, doi:10.1111/jace.16842.
[50] T. Wang, H. Chen, Z. Yang, J. Liang, S. Dai, High-entropy perovskite fluorides: a new platform for oxygen evolution catalysis, J. Am. Chem. Soc. (2020), doi:10.1021/jacs.9b12377.
[51] C. Heng, X. Huimin, D. Fu-Zhi, L. Jiachen, Z. Yanchun, High entropy (Yb0.25Y0.25Lu0.25Er0.25)2SiO5 with strong anisotropy in thermal expansion, J. Mater. Sci. Technol. (2019), doi:10.1016/j.jmst.2019.07.022.
[52] X. Ren, Z. Tian, J. Zhang, J. Wang, Equiatomic quaternary (Y1/4Ho1/4Er1/4Yb1/4)2SiO5 silicate: a perspective multifunctional thermal and environmental barrier coating material, Scr. Mater. 168 (2019) 47–50, doi:10.1016/j.scriptamat.2019.04.018.
[53] Y. Dong, K. Ren, Y. Lu, Q. Wang, J. Liu, Y. Wang, High-entropy environmental barrier coating for the ceramic matrix composites, J. Eur. Ceram. Soc. 39 (2019) 2574–2579, doi:10.1016/j.jeurceramsoc.2019.02.022.
[54] L. Sun, Y. Luo, X. Ren, Z. Gao, T. Du, Z. Wu, J. Wang, A multicomponent γ-type (Gd1/6Tb1/6Dy1/6Tm1/6Yb1/6Lu1/6)2Si2O7 disilicate with outstanding thermal stability, Mater. Res. Lett. 8 (2020) 424–430, doi:10.1080/21663831.2020.1783007.
[55] Z. Zhao, H. Chen, H. Xiang, F.Z. Dai, X. Wang, Z. Peng, Y. Zhou, $(La_{0.2}Ce_{0.2}Nd_{0.2}Sm_{0.2}Eu_{0.2})PO_4$: a high-entropy rare-earth phosphate monazite ceramic with low thermal conductivity and good compatibility with Al_2O_3, J. Mater. Sci. Technol. 35 (2019) 2892–2896, doi:10.1016/j.jmst.2019.08.012.
[56] Z. Zhao, H. Xiang, F.Z. Dai, Z. Peng, Y. Zhou, (TiZrHf)P2O7: an equimolar multicomponent or high entropy ceramic with good thermal stability and low thermal conductivity, J. Mater. Sci. Technol. 35 (2019) 2227–2231, doi:10.1016/j.jmst.2019.05.030.
[57] N. Qiu, H. Chen, Z. Yang, S. Sun, Y. Wang, Y. Cui, A high entropy oxide (Mg0.2Co0.2Ni0.2Cu0.2Zn0.2O) with superior lithium storage performance, J. Alloy. Compd. 777 (2019) 767–774, doi:10.1016/j.jallcom.2018.11.049.
[58] Q. Wang, A. Sarkar, Z. Li, Y. Lu, L. Velasco, S.S. Bhattacharya, T. Brezesinski, H. Hahn, B. Breitung, High entropy oxides as anode material for Li-ion battery applications: a practical approach, Electrochem. Commun. 100 (2019) 121–125, doi:10.1016/j.elecom.2019.02.001.
[59] A. Sarkar, L. Velasco, D. Wang, Q. Wang, G. Talasila, L. de Biasi, C. Kübel, T. Brezesinski, S.S. Bhattacharya, H. Hahn, B. Breitung, High entropy oxides for reversible energy storage, Nat. Commun. 9 (2018) 3400, doi:10.1038/s41467-018-05774-5.
[60] B. Breitung, Q. Wang, A. Schiele, Đ. Tripković, A. Sarkar, L. Velasco, D. Wang, S.S. Bhattacharya, H. Hahn, Breze, Gassing behavior of high-entropy oxide anode and oxyfluoride cathode probed using differential electrochemical mass spectrometry, Batter. Supercaps. (n.d.). doi:10.1002/batt.202000010.
[61] A.G. de la Obra, M.A. Avilés, Y. Torres, E. Chicardi, F.J. Gotor, A new family of cermets: chemically complex but microstructurally simple, Int. J. Refract. Met. Hard Mater. 63 (2017) 17–25, doi:10.1016/j.ijrmhm.2016.04.011.
[62] J. Gild, A. Wright, K. Quiambao-tomko, M. Qin, A. John, S. Hoque, J.L. Braun, B. Bloomfield, D. Martinez, T. Harrington, K. Vecchio, P.E. Hopkins, J. Luo, Thermal conductivity and hardness of three single-phase high-entropy metal diborides fabricated by borocarbothermal reduction and spark plasma sintering, Ceram. Int. (2019), doi:10.1016/j.ceramint.2019.11.186.
[63] H. Zhang, D. Hedman, P. Feng, G. Han, F. Akhtar, A high-entropy B4(HfMo2TaTi)C and SiC ceramic composite, Dalt. Trans. 48 (2019) 5161–5167, doi:10.1039/c8dt04555k.
[64] P. Sarker, T. Harrington, C. Toher, C. Oses, M. Samiee, J.P. Maria, D.W. Brenner, K.S. Vecchio, S. Curtarolo, High-entropy high-hardness metal carbides discovered by entropy descriptors, Nat. Commun. 9 (2018) 1–10, doi:10.1038/s41467-018-07160-7.
[65] K. Kaufmann, D. Maryanovsky, W.M. Mellor, C. Zhu, A.S. Rosengarten, T.J. Harrington, C. Oses, C. Toher, S. Curtarolo, K.S. Vecchio, Discovery of high-entropy ceramics via machine learning, Npj Comput. Mater. 6 (2020) 42, doi:10.1038/s41524-020-0317-6.
[66] A. Giri, J.L. Braun, P.E. Hopkins, Reduced dependence of thermal conductivity on temperature and pressure of multi-atom component crystalline solid solutions, J. Appl. Phys. 123 (2018) 015106, doi:10.1063/1.5010337.
[67] A. Giri, J.L. Braun, C.M. Rost, P.E. Hopkins, On the minimum limit to thermal conductivity of multi-atom component crystalline solid solutions based on impurity mass scattering, Scr. Mater. 138 (2017) 134–138, doi:10.1016/j.scriptamat.2017.05.045.
[68] A.J. Wright, Q. Wang, C. Hu, Y.T. Yeh, R. Chen, J. Luo, Single-phase duodenary high-entropy fluorite/pyrochlore oxides with an order-disorder transition, Acta Mater (2021) 116858, doi:10.1016/j.actamat.2021.116858.
[69] K. Ren, Q. Wang, G. Shao, X. Zhao, Y. Wang, Multicomponent high-entropy zirconates with comprehensive properties for advanced thermal barrier coating, Scr. Mater. 178 (2020) 382–386, doi:10.1016/j.scriptamat.2019.12.006.
[70] J.L. Braun, C.M. Rost, M. Lim, A. Giri, D.H. Olson, G.N. Kotsonis, G. Stan, D.W. Brenner, J.P. Maria, P.E. Hopkins, Charge-induced disorder controls the thermal conductivity of entropy-stabilized oxides, Adv. Mater. 30 (2018) 1805004, doi:10.1002/adma.201805004.
[71] H. Chen, Z. Zhao, H. Xiang, F.Z. Dai, W. Xu, K. Sun, J. Liu, Y. Zhou, High entropy $(Y_{0.2}Yb_{0.2}Lu_{0.2}Eu_{0.2}Er_{0.2})3Al_5O_{12}$: a novel high temperature stable thermal barrier material, J. Mater. Sci. Technol. (2020), doi:10.1016/j.jmst.2020.01.056.
[72] Z. Zhao, H. Xiang, F.Z. Dai, Z. Peng, Y. Zhou, $(La_{0.2}Ce_{0.2}Nd_{0.2}Sm_{0.2}Eu_{0.2})2Zr_2O_7$: a novel high-entropy ceramic with low thermal conductivity and sluggish grain growth rate, J. Mater. Sci. Technol. 35 (2019) 2647–2651, doi:10.1016/j.jmst.2019.05.054.
[73] J. Zhu, X. Meng, J. Xu, P. Zhang, Z. Lou, M.J. Reece, F. Gao, Ultra-low thermal conductivity and enhanced mechanical properties of high-entropy rare earth niobates (Re_3NbO_7, *Re*=Dy, Y, Ho, Er, Yb), J. Eur. Ceram. Soc. (2020), doi:10.1016/j.psyneuen.2020.104810.
[74] L. Chen, Y. Wang, M. Hu, L. Zhang, J. Wang, Z. Zhang, X. Liang, J. Guo, J. Feng, Achieved limit thermal conductivity and enhancements of mechanical properties in fluorite RE 3 NbO 7 via entropy engineering, Appl. Phys. Lett. 118 (2021) 071905, doi:10.1063/5.0037373.
[75] G. King, C.M. Thompson, J.E. Greedan, A. Llobet, Local structure of the vacancy disordered fluorite Yb_3TaO_7 from neutron total scattering, J. Mater. Chem. A 1 (2013) 10487–10494, doi:10.1039/c3ta12100c.
[76] P.B. Allen, J.L. Feldman, J. Fabian, F. Wooten, Diffusons, locons and propagons: character of atomic vibrations in amorphous Si, Philos. Mag. B 79 (1999) 1715–1731, doi:10.1080/13642819908223054.
[77] ASTM InternationalC373-18 Standard Test Methods for Determination of Water Absorption and Associated Properties By Vacuum Method for Pressed Ceramic Tiles and Glass Tiles and Boil Method for Extruded Ceramic Tiles and Non-tile Fired Ceramic Whiteware Products, ASTM International, West Conshohocken, PA, 2018, doi:10.1520/C0373-16.2.
[78] ASTM InternationalC1198-20 Standard Test Method for Dynamic Young's Modulus, Shear Modulus, and Poisson's Ratio for Advanced Ceramics by Sonic Resonance, ASTM International, West Conshohocken, PA, 2020, doi:10.1520/C1198-20.
[79] E.A. Dean, J.A. Lopez, Empirical dependence of elastic moduli on porosity for ceramic materials, J. Am. Ceram. Soc. 66 (1983) 366–370, doi:10.1111/j.1151-2916.1983.tb10051.x.
[80] I. Barin, Thermochemical Data of Pure Substances, VCH, Weinheim, 1995, doi:10.1016/s0165-2427(96)05632-2.
[81] R.W. Rice, Porosity of Ceramics: Properties and Applications, CRC Press, 1998, doi:10.1017/CBO9781107415324.004.
[82] C.L. Farrow, P. Juhas, J.W. Liu, D. Bryndin, E.S. Boin, J. Bloch, T. Proffen, S.J.L. Billinge, PDFfit2 and PDFgui: computer programs for studying nanostructure in crystals, J. Phys. Condens. Matter. 19 (2007) 335219, doi:10.1088/0953-8984/19/33/335219.
[83] K. Momma, F. Izumi, VESTA 3 for three-dimensional visualization of crystal, volumetric and morphology data, J. Appl. Crystallogr. 44 (2011) 1272–1276, doi:10.1107/S0021889811038970.
[84] J. Yang, X. Qian, W. Pan, R. Yang, Z. Li, Y. Han, M. Zhao, M. Huang, C. Wan, Diffused lattice vibration and ultralow thermal conductivity in the binary Ln–Nb–O oxide system, Adv. Mater. 31 (2019) 1808222, doi:10.1002/adma.201808222.
[85] R.D. Shannon, Revised effective ionic radii and systematic studies of interatomic distances in halides and chalcogenides, Acta Crystallogr. Sect. A 32 (1976) 751–767, doi:10.1107/S0567739476001551.
[86] F. Wu, P. Wu, R. Zong, J. Feng, Investigation on thermo-physical and mechanical properties of $Dy_3(Ta1\text{-}xNbx)O_7$ ceramics with order-disorder transition, Ceram. Int. 45 (2019) 15705–15710, doi:10.1016/j.ceramint.2019.04.207.
[87] Y. Doi, Y. Harada, Y. Hinatsu, Crystal structures and magnetic properties of fluorite-related oxides Ln_3NbO_7 (Ln=lanthanides), J. Solid State Chem. 182 (2009) 709–715, doi:10.1016/j.jssc.2008.12.012.
[88] 琳陈, 晶冯, 稀土钽酸盐RE3TaO7和RETa3O9陶瓷 热-力学性质研究进展, J. Adv. Ceram. 40 (2019) 367–397.
[89] L. Chen, P. Wu, J. Feng, Optimization thermophysical properties of TiO_2 alloying Sm_3TaO_7 ceramics as promising thermal barrier coatings, Int. J. Appl. Ceram. Technol. 16 (2019) 230–242, doi:10.1111/ijac.13079.
[90] L. Chen, J. Guo, Y. Zhu, M. Hu, J. Feng, Features of crystal structures and thermo-mechanical properties of weberites $RE3NbO_7$ (RE=La, Nd, Sm, Eu, Gd) ceramics, J. Am. Ceram. Soc. (2020), doi:10.1111/jace.17437.
[91] F. DeAngelis, M.G. Muraleedharan, J. Moon, H.R. Seyf, A.J. Minnich, A.J.H. McGaughey, A. Henry, Thermal transport in disordered materials, Nanoscale Microscale Thermophys. Eng. 23 (2019) 81–116, doi:10.1080/15567265.2018.1519004.
[92] S. Shin, Q. Wang, J. Luo, R. Chen, Advanced materials for high-temperature thermal transport, Adv. Funct. Mater. (2019) 1904815, doi:10.1002/adfm.201904815.
[93] W. Zhou, Y. Cheng, K. Chen, G. Xie, T. Wang, G. Zhang, Thermal conductivity of amorphous materials, Adv. Funct. Mater. (2019) 1903829, doi:10.1002/adfm.201903829.
[94] D.G. Cahill, S.K. Watson, R.O. Pohl, Lower limit to the thermal conductivity of disordered crystals, Phys. Rev. B 46 (1992) 6131–6140, doi:10.1103/PhysRevB.46.6131.
[95] Y. Luo, X. Yang, T. Feng, J. Wang, X. Ruan, Vibrational hierarchy leads to dual-phonon transport in low thermal conductivity crystals, Nat. Commun. 11 (2020) 2554, doi:10.1038/s41467-020-16371-w.
[96] M.T. Agne, R. Hanus, G.J. Snyder, Minimum thermal conductivity in the context of: diffuson-mediated thermal transport, Energy Environ. Sci. 11 (2018) 609–616, doi:10.1039/c7ee03256k.
[97] A.R. Overy, A. Simonov, P.A. Chater, M.G. Tucker, A.L. Goodwin, Phonon broadening from supercell lattice dynamics: random and correlated disorder, Phys. Status Solidi Basic Res. 254 (2017), doi:10.1002/pssb.201600586.
[98] A.R. Overy, A.B. Cairns, M.J. Cliffe, A. Simonov, M.G. Tucker, A.L. Goodwin, De-

sign of crystal-like aperiodic solids with selective disorder-phonon coupling, Nat. Commun. 7 (2016) 1–8, doi:10.1038/ncomms10445.
[99] D.A. Keen, A.L. Goodwin, The crystallography of correlated disorder, Nature 521 (2015) 303–309, doi:10.1038/nature14453.
[100] J.G. Allpress, H.J. Rossell, Fluorite-related phases Ln_3MO_7, Ln = rare earth, Y, or *Sc*, M = Nb, Sb, or Ta. I. Crystal chemistry, J. Solid State Chem. 27 (1979) 105–114, doi:10.1016/0022-4596(79)90149-X.
[101] J. Luo, Stabilization of nanoscale quasi-liquid interfacial films in inorganic materials: a review and critical assessment, Crit. Rev. Solid State Mater. Sci. 32 (2007) 67–109.
[102] D.R. Clarke, On the equilibrium thickness of intergranular glass phases in ceramic materials, J. Am. Ceram. Soc. 70 (1987) 15–22, doi:10.1111/j.1151-2916.1987.tb04846.x.
[103] J. Luo, Liquid-like interface complexion: from activated sintering to grain boundary diagrams, Curr. Opin. Solid State Mater. Sci. 12 (2008) 81–88.
[104] J. Luo, Origin of solid-state activated sintering in Bi_2O_3-doped ZnO, J. Am. Ceram. Soc. 82 (1999) 916–920, doi:10.1111/j.1151-2916.1999.tb01853.x.
[105] J. Luo, V.K. Gupta, D.H. Yoon, H.M. Meyer, Segregation-induced grain boundary premelting in nickel-doped tungsten, Appl. Phys. Lett. 87 (2005) 231902.
[106] V.K. Gupta, D.H. Yoon, H.M. Meyer, J. Luo, Thin intergranular films and solid-state activated sintering in nickel-doped tungsten, Acta Mater. 55 (2007) 3131–3142.
[107] X. Shi, J. Luo, Grain boundary wetting and prewetting in Ni-doped Mo, Appl. Phys. Lett. 94 (2009) 251908.
[108] T. Hu, S. Yang, N. Zhou, Y. Zhang, J. Luo, Role of disordered bipolar complexions on the sulfur embrittlement of nickel general grain boundaries, Nat. Commun. 9 (2018) 2764, doi:10.1038/s41467-018-05070-2.
[109] J. Luo, Y.M. Chiang, Wetting and prewetting on ceramic surfaces, Annu. Rev. Mater. Res. 38 (2008) 227–249.
[110] J. Luo, Y.M. Chiang, Equilibrium-thickness amorphous films on {1120} surfaces of Bi_2O_3-doped ZnO, J. Eur. Ceram. Soc. 19 (1999) 697–701.
[111] J. Luo, Y.M. Chiang, Existence and stability of nanometer-thick disordered films on oxide surfaces, Acta Mater. 48 (2000) 4501–4515.
[112] J. Luo, Y.M. Chiang, R.M. Cannon, Nanometer-thick surficial films in oxides as a case of prewetting, Langmuir 21 (2005) 7358–7365.
[113] A. Kayyar, H. Qian, J. Luo, Surface adsorption and disordering in LiFePO4 based battery cathodes, Appl. Phys. Lett. 95 (2009) 221905.
[114] H. Qian, J. Luo, Vanadia-based equilibrium-thickness amorphous films on anatase (101) surfaces, Appl. Phys. Lett. 91 (2007) 61909.
[115] H. Qian, J. Luo, Nanoscale surficial films and a surface transition in V_2O_5–TiO_2-based ternary oxide systems, Acta Mater. 56 (2008) 4702–4714.
[116] J. Nie, J.M. Chan, M. Qin, N. Zhou, J. Luo, Liquid-like grain boundary complexion and sub-eutectic activated sintering in CuO-doped TiO_2, Acta Mater. 130 (2017) 329–338.
[117] J. Luo, Developing interfacial phase diagrams for applications in activated sintering and beyond: current status and future directions, J. Am. Ceram. Soc. 95 (2012) 2358–2371.
[118] P.R. Cantwell, M. Tang, S.J. Dillon, J. Luo, G.S. Rohrer, M.P. Harmer, Grain boundary complexions, Acta Mater. 62 (2014) 1–48.
[119] S.J. Dillon, M. Tang, W.C. Carter, M.P. Harmer, Complexion: a new concept for kinetic engineering in materials science, Acta Mater. 55 (2007) 6208–6218.
[120] J. Nie, C. Hu, Q. Yan, J. Luo, Discovery of electrochemically induced grain boundary transitions, Nat. Commun. 12 (2021) 1–10, doi:10.1038/s41467-021-22669-0.
[121] S. Ma, K.M. Asl, C. Tansarawiput, P.R. Cantwell, M. Qi, M.P. Harmer, J. Luo, A grain boundary phase transition in Si–Au, Scr. Mater. 66 (2012) 203–206.
[122] S. Ma, P.R. Cantwell, T.J. Pennycook, N. Zhou, M.P. Oxley, D.N. Leonard, S.J. Pennycook, J. Luo, M.P. Harmer, Grain boundary complexion transitions in WO_3-and CuO-doped TiO_2 bicrystals, Acta Mater. 61 (2013) 1691–1704.
[123] W. Cao, C. Marvel, D. Yin, Y. Zhang, P. Cantwell, M.P. Harmer, J. Luo, R.P. Vinci, Correlations between microstructure, fracture morphology, and fracture toughness of nanocrystalline Ni–W alloys, Scr. Mater. 113 (2016) 84–88.
[124] P.R. Cantwell, T. Frolov, T.J. Rupert, A.R. Krause, C.J. Marvel, G.S. Rohrer, J.M. Rickman, M.P. Harmer, Grain boundary complexion transitions, Annu. Rev. Mater. Res. 50 (2020) 465–492.
[125] N. Zhou, C. Hu, J. Luo, Grain boundary segregation transitions and critical phenomena in binary regular solutions: a systematics of complexion diagrams with universal characters, Acta Mater. 221 (2021) 117375, doi:10.1016/j.actamat.2021.117375.
[126] E.C. O'Quinn, K.E. Sickafus, R.C. Ewing, G. Baldinozzi, J.C. Neuefeind, M.G. Tucker, A.F. Fuentes, D. Drey, M.K. Lang, Predicting short-range order and correlated phenomena in disordered crystalline materials, Sci. Adv. 6 (2020) eabc2758, doi:10.1126/sciadv.abc2758.
[127] D.L. Drey, E.C. O'Quinn, T. Subramani, K. Lilova, G. Baldinozzi, I.M. Gussev, A.F. Fuentes, J.C. Neuefeind, M. Everett, D. Sprouster, A. Navrotsky, R.C. Ewing, M. Lang, Disorder in $Ho_2Ti_2{-}xZrxO_7$: pyrochlore to defect fluorite solid solution series, RSC Adv. 10 (2020) 34632–34650, doi:10.1039/D0RA07118H.
[128] A.F. Fuentes, S.M. Montemayor, M. Maczka, M. Lang, R.C. Ewing, U. Amador, A critical review of existing criteria for the prediction of pyrochlore formation and stability, Inorg. Chem. 57 (2018) 12093–12105, doi:10.1021/acs.inorgchem.8b01665.
[129] I.M. Gussev, E.C. O'Quinn, G. Baldinozzi, J. Neuefeind, R.C. Ewing, F. Zhang, M. Lang, Local order of orthorhombic weberite-type Y_3TaO_7 as determined by neutron total scattering and density functional theory calculations, Acta Mater. 196 (2020) 704–709, doi:10.1016/j.actamat.2020.07.005.
[130] J. Shamblin, M. Feygenson, J. Neuefeind, C.L. Tracy, F. Zhang, S. Finkeldei, D. Bosbach, H. Zhou, R.C. Ewing, M. Lang, Probing disorder in isometric pyrochlore and related complex oxides, Nat. Mater. 15 (2016) 507–511, doi:10.1038/nmat4581.